Circulation Research

ORIGINAL RESEARCH

An Alternative Mechanism of Subcellular Iron Uptake Deficiency in Cardiomyocytes

Yuanyuan Dai, Nadezda Ignatyeva, Hang Xu, Ruheen Wali, Karl Toischer, Sören Brandenburg, Christof Lenz, Julius Pronto, Funsho E. Fakuade, Samuel Sossalla, Elisabeth M. Zeisberg, Andreas Janshoff, Ingo Kutschka, Niels Voigt, Henning Urlaub, Torsten Bloch Rasmussen, Jens Mogensen, Stephan E. Lehnart, Gerd Hasenfuss, Antje Ebert

BACKGROUND: Systemic defects in intestinal iron absorption, circulation, and retention cause iron deficiency in 50% of patients with heart failure. Defective subcellular iron uptake mechanisms that are independent of systemic absorption are incompletely understood. The main intracellular route for iron uptake in cardiomyocytes is clathrin-mediated endocytosis.

METHODS: We investigated subcellular iron uptake mechanisms in patient-derived and CRISPR/Cas–edited induced pluripotent stem cell–derived cardiomyocytes as well as patient-derived heart tissue. We used an integrated platform of DIA-MA (mass spectrometry data-independent acquisition)–based proteomics and signaling pathway interrogation. We employed a genetic induced pluripotent stem cell model of 2 inherited mutations (*TnT* [*troponin T*]-R141W and *TPM1* [*tropomyosin 1*]-L185F) that lead to dilated cardiomyopathy (DCM), a frequent cause of heart failure, to study the underlying molecular dysfunctions of DCM mutations.

RESULTS: We identified a druggable molecular pathomechanism of impaired subcellular iron deficiency that is independent of systemic iron metabolism. Clathrin-mediated endocytosis defects as well as impaired endosome distribution and cargo transfer were identified as a basis for subcellular iron deficiency in DCM-induced pluripotent stem cell–derived cardiomyocytes. The clathrin-mediated endocytosis defects were also confirmed in the hearts of patients with DCM with end-stage heart failure. Correction of the *TPM1-L185F* mutation in DCM patient–derived induced pluripotent stem cells, treatment with a peptide, Rho activator II, or iron supplementation rescued the molecular disease pathway and recovered contractility. Phenocopying the effects of the *TPM1-L185F* mutation into WT induced pluripotent stem cell–derived cardiomyocytes could be ameliorated by iron supplementation.

CONCLUSIONS: Our findings suggest that impaired endocytosis and cargo transport resulting in subcellular iron deficiency could be a relevant pathomechanism for patients with DCM carrying inherited mutations. Insight into this molecular mechanism may contribute to the development of treatment strategies and risk management in heart failure.

GRAPHIC ABSTRACT: A graphic abstract is available for this article.

Key Words: cardiomyopathy, dilated ■ cardiovascular disease ■ heart failure ■ iron deficiency ■ sarcomere

In This Issue, see p 105 | Meet the First Author, see p 106

Iron deficiency is a frequent comorbidity in heart failure (HF) affecting 50% of patients with HF[1,2] and has been linked to cardiovascular disease as well.[3–5] The physiological basis of iron deficiency has been described by duodenal blockage of iron absorption, iron retention in the reticuloendothelial system, as well as circulation-related absorption defects.[2,6] Long-term intravenous iron therapy showed beneficial effects to patients with HF in clinical trials[4,7–10] and compensation of iron levels reduces morbidity and mortality. In contrast, the subcellular iron uptake mechanisms that are independent of systemic absorption, as well as the adverse consequences of defects in these processes are incompletely understood. Subcellular iron uptake occurs by clathrin-mediated endocytosis (CME) of the iron carrier protein transferrin.[11,12] An essential step for initiation of CME events is the formation of plasma

Correspondence to: Antje Ebert, PhD, Goettingen University Medical Center, Goettingen University, Robert-Koch-Strasse 40, 37075 Goettingen, Germany. Email antje.ebert@med.uni-goettingen.de
Supplemental Material is available at https://www.ahajournals.org/doi/suppl/10.1161/CIRCRESAHA.122.321157.
For Disclosures, see page e43.

Circulation Research is available at www.ahajournals.org/journal/res

Novelty and Significance

What Is Known?

- Iron deficiency due to systemic defects in intestinal iron absorption, circulation, and retention occurs frequently in heart failure.
- Clathrin-mediated endocytosis (CME) is the main route for uptake of critical subcellular cargo, such as transferrin-bound iron, into cardiomyocytes.
- Sarcomere protein mutations frequently lead to dilated cardiomyopathy (DCM); the underlying molecular dysfunctions are incompletely understood.

What New Information Does This Article Contribute?

- We applied a multi-layered, integrational molecular platform for signaling pathway interrogation to decipher molecular dysfunctions of DCM mutations in sarcomere proteins.
- We identified a druggable molecular pathomechanism, specifically, defective CME-dependent signaling resulting in impaired subcellular iron uptake, that is independent of systemic iron metabolism. These molecular defects were recapitulated in the hearts of patients with DCM with end-stage heart failure.
- Correction of the *TPM1* (*tropomyosin 1*)-*L185F* mutation in DCM patient–derived iPSCs, treatment with a small peptide, RhoA II, or iron supplementation rescued the molecular disease pathway and recovered contractility.

Utilizing label-free DIA-MS (mass spectrometry data-independent acquisition) whole-proteome analysis enabled us to perform pathway mapping for a novel DCM mutation, *TPM1-L185F*, in DCM patient–derived and CRISPR/Cas genome edited induced pluripotent stem cell–derived cardiomyocytes. We identified CME defects as well as impaired endosome distribution and cargo transfer as a new basis for mitochondrial iron deficiency in the presence of different DCM mutations. Isogenic mutation-introduced induced pluripotent stem cell–derived cardiomyocytes recapitulated endocytosis defects, impaired endosome distribution, and mitochondrial iron deficiency as well as mitochondrial dysfunction. We could also confirm the CME defects in the hearts of patients with DCM with end-stage heart failure. CRISPR/Cas–based genomic correction of the *TPM1-L185F* mutation in DCM patient–derived iPSCs rescued the molecular disease pathway in isogenic induced pluripotent stem cell–derived cardiomyocytes. Phenocopying the effects of the *TPM1-L185F* mutation into WT induced pluripotent stem cell–derived cardiomyocytes could be ameliorated by iron supplication and treatment with a small peptide, RhoA II. We found that therapeutic targeting of defective endocytosis and iron levels recovered contractility to the levels observed in healthy donors. Therefore, RhoA II and other drug treatments targeting endocytosis defects that cause iron deficiency could be considered promising therapeutic directions for DCM and heart failure.

Nonstandard Abbreviations and Acronyms

CME	clathrin-mediated endocytosis
DCM	dilated cardiomyopathy
DMT1	divalent metal transporter 1
EE	early endosome
HD	healthy donor
iPSC-CMs	induced pluripotent stem cell–derived cardiomyocytes
IRP/IRE	iron-responsive protein/iron-responsive element
Lat-A	latrunculin A
Mut-cor	mutation-corrected
PIP2	phosphatidylinositol 4,5-bisphosphate
PM	plasma membrane
RhoA II	Rho activator II
SAA	sarcomeric alpha-actinin
TfR1	transferrin receptor 1
TnT	troponin T
TPM	tropomyosin

membrane (PM) microdomain hubs enriched for phosphatidylinositol 4,5-bisphosphate (PIP2) and fibrous actin (F-actin).[13,14] Importantly, decreased F-actin content at the PM of cardiomyocytes from patients with dilated cardiomyopathy (DCM) with end-stage HF has been highlighted as a critical disease feature in myocardial dysfunction.[15] Moreover, loss-of-function mutations in cytoskeletal proteins are known to contribute to alteration of the actin cytoskeleton and the progression of DCM and HF in humans.[16–18] Nevertheless, the understanding of subcellular dysfunctions in presence of inherited DCM mutations remains incomplete.

To better understand the molecular disease mechanisms associated with DCM mutations, we employed a genetic induced pluripotent stem cell (iPSC) model of 2 inherited mutations in recognized DCM genes, *TnT* (*troponin T, TNNT2, R141W*) and *TPM1* (*tropomyosin 1, L185F*). Interestingly, we found defective intracellular iron uptake in iPSC-derived cardiomyocytes from patients with DCM with inherited mutations. The defective iron uptake was due to disrupted sarcomere organization in DCM cardiomyocytes which impaired the linkage and formation of F-actin–enriched PM microdomains as a basis for CME-mediated iron uptake.

DCM is a major cause of HF and is characterized clinically by ventricular dilation and contractile dysfunction.[19] Inherited mutations, frequent causes of DCM affecting 30% of patients,[20] presented a basis for disease modeling using human iPSC–derived cardiomyocytes (HiPSCs). Human iPSC-CMs have been employed to study causes of subcellular disease phenotypes in DCM[21–23] such as disrupted sarcomere protein organization and defective contractility. Goal of this study was to identify druggable pathogenic molecular signaling defects altered in the presence of DCM mutations due to defective sarcomere organization and function. We utilized 2 different DCM iPSC models, the troponin mutation *TnT-R141W*[24–26] and a novel DCM-causing variant, *TPM1-L185F*. TPM1, a critical regulator of force generation in cardiomyocytes, anchors the troponin complex on actin myofilaments.[27–30] Previous reports demonstrated the pathogenicity of *TPM1* mutations in DCM, which reduce force generation and Ca^{2+} sensitivity of cardiomyocytes.[31–33] *TPM1-L185F* is located in a mutational hot spot of TPM1 within the troponin complex-interacting region.[27,30] Due to their location, the DCM mutations *TPM1-L185F* as well as *TnT-R141W* were likely to disrupt sarcomere function. Accordingly, the DCM *TPM1-L185F* patient–specific and CRISPR/Cas9 mutation–introduced iPSC-CMs displayed altered sarcomere organization, contractility, and force generation as well as cytoskeleton filament interactions.

Here, we identified a molecular pathway altered in DCM cardiomyocytes due to defective sarcomere organization and function, which is present in DCM models but also in the heart tissues of patients with other forms of systolic HF. We show a new mechanistic defect in iron uptake in DCM cardiomyocytes, which results in subcellular iron deficiency and mitochondrial iron-depletion dysfunctions. This pathway is not related to physiological and systemic iron absorption defects in HF.

Our findings show that sarcomere disorganization in DCM cardiomyocytes disrupted vinculin-based linkage and formation of PM hubs enriched for F-actin and PIP2. Consequently, disruption of PM microdomains limited the initiation of endocytosis and thereby reduced the uptake of critical cargo such as transferrin-bound iron. Particularly in the mitochondria, iron imbalance is deleterious as mitochondrial functions require fine-balanced iron levels.[34] Both the inappropriate elevation as well as reduction of iron levels are associated with cardiac disease.[34,35] Previous studies showed that in the murine heart, lack of TfR1 (transferrin receptor 1), the key iron transport protein, resulted in severely reduced iron levels in cardiomyocytes, causing poor cardiac function and failure of mitochondrial respiration.[36] In this study, we describe a molecular regulatory pathomechanism that depletes intracellular iron levels in cardiomyocytes carrying DCM mutations. We employed CRISPR/Cas9 genome editing together with whole-proteome mapping technologies and delivered genetic and pharmacological rescue strategies to reverse the molecular pathway´s dysfunction. CRISPR/Cas9–based correction of the DCM mutation, resupplementation of iron, or treatment with a small peptide molecule (RhoA activator II) rescued endosome distribution, mitochondrial iron levels, contractility, and sarcomere protein organization in iPSC-CMs.

We confirmed that this molecular disease pathway is not limited to DCM iPSC-CMs but occurs also in the heart tissue of patients with DCM with end-stage HF. Therefore, defective endocytosis and impaired endosome distribution may present pathogenic and functional defects that are more generally representative of DCM and systolic HF. Our approach to therapeutically target the molecular defects in this pathway may suggest an alternative opportunity for development of future treatment directions in patients with DCM and HF due to inherited mutations.

METHODS

Data Availability

The authors declare that all supporting data are available within the article and in the Supplemental Material. A detailed description of the Methods is available in the Supplemental Material. The data supporting the findings of this study and analytical tools are available from the corresponding author upon reasonable request. Please see the Major Resources Table in the Supplemental Material.

Generation, Culture, and Cardiac Differentiation of Human iPSCs

The protocols for studies with iPSC were approved by the Goettingen University Ethical Board (15/2/20 and 20/9/16An) and the Odense University Ethical Board (Projekt ID S-20140073HLP). Informed consent was obtained from all participants and all research was performed in accordance with relevant guidelines and regulations. Approval for the study of human myocardial samples was granted by the Goettingen University Ethical Board (No. 21/10/00 and 31/9/00), and written informed consent was obtained from all patients. The procedures used in this study adhere to the tenets of the Declaration of Helsinki. A family cohort with carriers of the novel pathogenic variant within the *TPM1* gene, *TPM1-L185F*, was recruited. Human fibroblasts from 5 mutation carriers and 4 healthy donors from this family were reprogrammed to hiPSCs using the CytoTune-iPS 2.0 Sendai Reprogramming Kit (Thermo Fisher Scientific). Human iPSCs were grown on Matrigel-coated plates (ES qualified, BD Biosciences) using chemically defined E8 medium as described previously.[37,38] The culture medium was changed every day, and iPSCs were passaged every 4 days using EDTA (Life Technologies). The iPSC lines have been deposited at the Goettingen University Medical Center Biobank or the Stanford Cardiovascular Institute Biobank. For cardiac differentiation of iPSCs, a small molecule-based monolayer protocol based on previous reports was utilized.[39,40] At day 20 to 25 of cardiac differentiation,

beating iPSC-CM cultures were dissociated using trypleE (Life Technologies) and plated in the required assay format. Human iPSC-CMs were cultured in Roswell Park Memorial Institute (RPMI; Life Technologies) complemented with B27 supplement (Life Technologies) before experimental analysis.

Liquid Chromatography/MS/MS DIA Analysis

Fifty micrograms of protein per sample were loaded onto a 4% to 12% NuPAGE Novex Bis-Tris Minigels (Invitrogen) and run into the gel for 1.5 cm. Following Coomassie staining, the protein areas were cut out, diced, and subjected to reduction with dithiothreitol, alkylation with iodoacetamide, and finally overnight digestion with trypsin. Tryptic peptides were extracted from the gel, the solution dried in a Speedvac, and kept at −20 °C for further analysis.[41]

Protein digests were analyzed on a nanoflow chromatography system (Eksigent nanoLC425) hyphenated to a hybrid triple quadrupole time-of-flight mass spectrometer (TripleTOF 5600+) equipped with a Nanospray III ion source (Ionspray Voltage 2400 V, Interface Heater Temperature 150 °C, Sheath Gas Setting 12) and controlled by Analyst TF 1.7.1 software build 1163 (all AB Sciex). In brief, peptides were dissolved in loading buffer (2% acetonitrile, 0.1% formic acid in water) to a concentration of 0.3 µg/uL. For each analysis, 1.5 µg protein were enriched on a self-packed precolumn (0.15 mm ID×20 mm, Reprosil-Pur120 C18-AQ 5 µm, Dr Maisch, Ammerbuch-Entringen, Germany) and separated on an analytical RP-C18 column (0.075 mm ID×200 mm, Reprosil-Pur 120 C18-AQ, 3 µm, Dr Maisch) using a 100-minute linear gradient of 5% to 35% acetonitrile/0.1% formic acid (v:v) at 300 nL min^{-1}.

Qualitative liquid chromatography/MS/MS analysis was performed using a Top 30 data-dependent acquisition method with an MS survey scan of m/z 380 to 1250 accumulated for 250 ms at a resolution of 35 000 full width at half maximum. MS/MS scans of m/z 180 to 1500 were accumulated for 100 ms at a resolution of 17 500 full width at half maximum and a precursor isolation width of 0.7 full width at half maximum, resulting in a total cycle time of 3.4 s. Precursors above a threshold MS intensity of 200 cps with charge states 2+, 3+, and 4+ were selected for MS/MS, the dynamic exclusion time was set to 15 s. MS/MS activation was achieved by CID using nitrogen as a collision gas and the manufacturer's default rolling collision energy settings. Two technical replicates per WT [wild type] and MUT [mutation] each were analyzed to construct a spectral library.

For quantitative DIA analysis, MS/MS data were acquired using 100 variable size windows[42] across the 400 to 1200 m/z range. Fragments were produced using rolling collision energy settings for charge state 2+, and fragments were acquired over an m/z range of 180 to 1500 for 40 ms per segment. Including a 250 ms survey scan, this resulted in an overall cycle time of 4.3 s. For WT and MUT groups, 2 technical replicates each were processed, and 2 replicated injection per sample were acquired, resulting in 4 samples per group.

Protein identification was achieved using ProteinPilot Software version 5.0 build 4304 (AB Sciex) at thorough settings. A total of 436 865 MS/MS spectra from the combined qualitative analyses were searched against the UniProtKB Homo sapiens reference proteome (revision 04-2016) augmented with a set of 51 known common laboratory contaminants.

DIA peak extraction was achieved in PeakView Software version 2.1 build 11041 (AB Sciex) using the DIA quantitation microApp version 2.0 build 2003. Following retention time correction on endogenous peptides spanning the entire retention time range, peak areas were extracted using information from the MS/MS library.[43] The resulting peak areas were then summed to peptide and finally protein area values, which were used for further statistical analysis. A nonparametric, Mann-Whitney *U* test was performed to establish statistical significance, as described earlier.[44]

F/G-Actin Measurements

Human iPSC-CMs were fixed in 4% paraformaldehyde for 20 minutes at room temperature following a PBS wash. Cells were incubated with 0.2% triton X-100 at room temperature for 60 minutes followed by a blocking step with 5% bovine serum albumin (BSA). Subsequently, cells were incubated with DnaseI-488 (Thermo Fisher Scientific), Phalloidin-488 (Thermo Fisher Scientific), DAPI (4′,6-diamidino-2-phenylindole)-405 (Thermo Fisher Scientific) according to the manufacturer´s description. Fluorescence was measured via a Cytation 3 reader (BioTek).

Atomic Force Microscopy and Contractility Measurements

iPSC-CMs were seeded on coverslips 2-3 days before atomic force microscopy or contractility measurements. Atomic force microscopy recordings were performed using a NanoWizard 3 (JPK Instruments) as described previously.[26] Briefly, the cantilever mounted on a glass block was dipped in cell medium for 30 to 60 minutes. A calibration was done to measure the spring constant and sensitivity of the used cantilever. The cells were probed with a nonconductive silicon nitride cantilever (Bruker). Contractility measurements were performed using an Olympus microscope with Olympus IX2-UCB software as described earlier.[23,26]

Drug Treatments

Human iPSC-CMs were treated with 3 µmol/L Latrunculin A (Cayman) for 20 minutes, UNC3230 (Cayman) 10 µmol/L for 24 hours, 3 µg/mL Rho activator II (Cytoskeleton) for 3 hours or overnight, and deferoxamine (Sigma-Aldrich) 80 µmol/L for 24 hours.

Sarcomere Length Analysis

iPSC-CMs were plated on coverslips and allowed to recover for 2 to 3 days. Cells were fixed by 4% paraformaldehyde and stained with TnT (rabbit; Thermo Fisher Scientific) and alpha-actinin (mouse, Sigma-Aldrich) as primary antibodies overnight at 4 °C. Anti-Mouse IgG1 Alexa Fluor 488 and anti-Rabbit IgG (H+L; heavy light chain) Alexa Fluor 568 were used as secondary antibodies to stain coverslips. Images were acquired under a ×63 objective (oil-immersed) at a confocal LSM710 microscope for the relevant channels. Image analysis was performed by ImageJ as described before.[23,26]

Contractility Measurements

iPSC-CMs were plated matrigel-coated 10 mm coverslips followed by recovery for 3 to 4 days. Analysis was done using a protocol described earlier.[23,26] Movies were recorded under a

×40 objective using an Olympus microscope with Olympus IX2-UCB software or a Basler camera with Pylon viewer software.

Colocalization Analysis of Vinculin and TnT

Human iPSC-CMs were plated on coverslips and allowed to recover for 2 to 3 days. Cells were fixed with 4% paraformaldehyde and stained with vinculin (mouse, Sigma-Aldrich) and TnT (rabbit, Abcam) primary antibodies overnight at 4 °C. Anti-Mouse IgG1 Alexa Fluor 488 and anti-Rabbit IgG (H+L) Alexa Fluor 568 were used as secondary antibodies to stain coverslips. Images were acquired under ×63 objective (oil-immersed) of a confocal LSM710 microscope for the relevant channels. The ImageJ plugin analyze particle was used to create regions of interest (ROIs) after setting automated thresholds within the TnT channel. ROIs were applied to the vinculin channel to measure mean fluorescence. Data were normalized for the vinculin-positive area in each cell.

PIP2 Quantification

Human iPSC-CMs were plated on coverslips and allowed to recover for 2 to 3 days. Fixed cells were stained with a PIP2-specific antibody (mouse, Echelon Biosciences) overnight at 4 °C and stained with secondary antibodies as described before.[45] Images were acquired under a ×63 objective at a confocal LSM710 microscope for the relevant channels. Line ROIs were drawn on the edge of cells using ImageJ, and mean fluorescence of the ROIs was quantified.

Immunohistochemistry of Adult Human Heart Tissue

The investigation conforms to the principles outlined in the Declaration of Helsinki. The institutional ethics committee approved the study, and all patients provided written informed consent for the use of cardiac tissue samples. Clinical data for patients are presented in Tables S2 and S3. Heart tissues from patients with dilated cardiomyopathy who received a heart transplantation due to end-stage heart failure (indicated as HF or heart transplantation) were analyzed. In comparison, LV heart tissue obtained during open-heart surgery from patients with preserved LV function that underwent aortic valve replacement (severe valve stenosis) and coronary artery bypass grafting was used in the control group (control). Explanted hearts or LV myocardial biopsies were directly put in precooled cardioprotective solution (Custodiol, Dr Franz Köhler Chemie, Bensheim, Germany; in mmol/L: NaCl 15, KCl 9, MgCl2 4, histidine hydrochloride monohydrate 18, histidine 180, tryptophan 2, mannitol 30, $CaCl_2$ 0.015, and potassium hydrogen 2-oxopentandiate 1). Subsequently, LV tissue samples were excised with scalpels and fixed in 4% paraformaldehyde overnight (Roti-Histofix 4 %, Carl Roth, Germany) before embedding in paraffin for immunohistology, or snap-frozen in liquid nitrogen before tissue lysis for immunoblotting (please see below). Human heart tissue slides were prepared and stained equally based on a previously published protocol.[46,47] Slides were incubated with primary antibodies overnight, such as TnT (rabbit; Thermo Fisher Scientific), vinculin (mouse, Sigma-Aldrich), or CCDC53 (rabbit; ProteinTech). WGA (Wheat germ agglutinin, Alexa Fluor 594 Conjugate; Thermo Fisher Scientific), 4′,6-diamidino-2-phenylindole (Thermo Fisher Scientific), and secondary antibodies such as Alexa Fluor 488 goat anti-Rabbit antibody (Thermo Fisher Scientific), Alexa Fluor 568 goat anti-Rabbit antibody (Thermo Fisher Scientific), Alexa Fluor 488 goat anti-mouse antibody (Thermo Fisher Scientific), were applied afterwards. Slides were mounted with FluroMount mounting medium (Thermo Fisher Scientific). Images were taken with ×63 (plan apochromat oil) objectives from a confocal microscope (Carl Zeiss, LSM 710, Göttingen, Germany) and ZEN software (Carl Zeiss). Controls for staining specificity were performed (Figure S14A through S14E). ImageJ-based analysis was used for image analysis. ImageJ was used to calculate the regularity of orientation for vinculin-positive structures. Data display the SEM of angles from vinculin-positive areas in each image. To analyze the location of CCDC53, automated threshold setting in WGA staining was used to define PM-localized ROIs. Data were normalized by the total CCDC53 signal per image.

Immunoblotting of Adult Human Heart Tissue

The investigation conforms to the principles outlined in the Declaration of Helsinki. The institutional ethics committee approved the study, and all patients provided written informed consent for the use of cardiac tissue samples. Human LV heart tissue (healthy controls) was obtained from freshly explanted hearts of 5 donor hearts that could not be transplanted due to clinical reasons.[48] Clinical data for 8 patients with DCM are presented in Tables S2 and S3. Lysates were obtained by homogenizing tissues at 4 °C for 5 minutes at 50 Hz in RIPA buffer (Thermo Fisher Scientific) with a metal bead (QIAGEN). Subsequently, lysates were incubated for 1 hour at 4 °C and supernatant was boiled at 100 °C for 10 minutes in sample buffer followed by SDS-PAGE and immunoblot analysis for WASL (WASP like actin nucleation promoting factor; rabbit, ProteinTech).

Tissue Procurement and Human Atrial Myocyte Isolation

For all patient samples, all experimental protocols were authorized by the ethics committee of the University Medical Center Göttingen (No. 4/11/18) and performed following the Declaration of Helsinki. Right atrial appendages were resected during routine cannulation of the right atrium (for extracorporeal circulation) of patients undergoing open-heart coronary bypass cardiac surgery. Excised tissues were immediately transported in a cardioplegic-based sterile transport solution (30 mM 2,3-butanedione monoxime, 20 mM glucose, 10 mM KCl, 1.2 mM KH_2PO_4, 5 mM $MgSO_4$, 5 mM MOPS, 100 mM NaCl, 50 mM taurine; pH 7.0) to the laboratory for atrial myocyte isolation using a previously described protocol.[49] Briefly, obtained atrial tissues were carefully trimmed of fat and minced into small pieces of ≈1 mm^3 in prechilled Ca^{2+}-free solution (20 mM glucose, 10 mM KCl, 1.2 mM KH_2PO_4, 5 mM $MgSO_4$, 5 mM MOPS, 100 mM NaCl, 50 mM taurine; pH 7.4). Minced tissues were then digested in Ca2+-free solution containing 286 U/mL collagenase type I (Worthington) and 5 U/mL protease XXIV (Sigma-Aldrich) enzymes for 45 minutes in a jacketed beaker with constant 100% O2 bubbling at 37 °C. After 10 minutes of digestion, $CaCl_2$ was introduced to attain a final concentration of 20 µM. After 45 minutes, a second digestion step was initiated using a new 20 mL Ca^{2+}-free solution containing 286 U/mL collagenase type I (Worthington) and 20 µM $CaCl_2$. Five minutes into tissue digestion, the supernatant was visualized under the microscope to detect dissociated myocytes. This process was repeated

every 3 minutes until dissociated myocytes were detected. Upon detection of myocytes, tissue chunks were retrieved and subjected to gentle mechanical trituration in a storage solution to dislodge myocytes. The resulting supernatant containing dissociated myocytes was strained with a nylon mesh and centrifugated at 90 g for 7 minutes to pellet the cells. Cell pellets were resuspended in fresh storage solution (1% w/v albumin, 10 mM glucose, 10 mM β-hydroxybutyric acid, 70 mM L-glutamic acid, 20 mM KCl, 10 mM KH2PO4, 10 mM taurine; pH 7.4 adjusted with 1 M KOH) and used for subsequent downstream experiments.

Statistical Analysis

Statistical significance was processed using GraphPad Prism v.8.4.2 (GraphPad) as well as Python scripts. Nonparametric tests including Mann-Whitney *U* test, Wilcoxon test, Kruskal-Wallis test, and Dunn multiple comparisons tests were applied to establish statistical significance. For 2 groups, a Mann-Whitney *U* test and Wilcoxon test (Figure 1G; Figure S7E) were used. For ≥3 groups, Kruskal-Wallis test and Dunn multiple comparisons tests were applied. $P<0.05$ were considered statistically significant. Data are presented as mean±SEM. Further information on statistical analysis, including the numbers of independent experiments performed for each figure, can be found in Table S5. However, the Mann-Whitney *U* test, Kruskal-Wallis, and Dunn multiple comparisons tests assume independent data sampling. These tests are not suitable to measure the statistical significance of data sets with dependent data sampling such as taking multiple measurements from independent rounds of iPSC cardiac differentiations. To address this limitation, in addition, a sensitivity analysis was performed in a lower-powered system, that is, nonparametric tests were carried out on averaged data points from independent cardiac differentiations to evaluate dependent data sampling. The results show a trend in the direction observed in the main analysis and are presented in Table S5. Unless indicated otherwise, the number of independent experiments used equals the number of independent iPSC cardiac differentiations.

Data Availability

A detailed description of the Methods is available in the Supplemental Material. The proteomics data can be found in the PRIDE (PRoteomics IDEntifications) repository under the project accession PXD040863.

The data, analytic methods, and study materials are available to other researchers for purposes of reproducing the results or replicating the procedures upon reasonable requests. Because of the sensitive nature of the data collected for this study, requests to access the dataset from qualified researchers may be sent to the corresponding author.

RESULTS

A TPM1 Mutation Causes Defective Contractility, Force Generation, and Sarcomere Connections with the PM in DCM Patient–Specific iPSC-CMs

We recruited a family cohort of patients with DCM carrying the point mutation *TPM1-L185F* which caused ventricular dilatation, sinus rhythm abnormalities, and nonsustained ventricular tachycardia in the patients (Figure 1A; Figure S1A through S1C). We generated iPSCs from a 15-year-old male carrier, III-5 (patient with DCM, MUT [mutation]/WT [wild type]) who received a heart transplantation due to end-stage HF, as well as from a nonaffected family member, II-4 (healthy donor, HD, WT/WT; Figure 1A; Figure S1A through S1C). WT/WT and WT/MUT iPSCs displayed regular expression of pluripotency markers (Figure S2A through S2E). We differentiated iPSCs into beating iPSC-CMs and found patient-specific (WT/MUT) and HD control (WT/WT) iPSC-CMs to express comparable levels of TPM1 and other cardiac markers at the gene expression and protein expression levels (Figure S3A through S3K). Patient-specific (WT/MUT) iPSC-CMs recapitulated reduced sarcomere length, beating force, and contractility, compared to HD control (WT/WT) iPSC-CMs (Figure 2B through 2E; Figure S4A through S4E). We also noted reduced field potential duration and amplitude in the presence of TPM1-L185F (Figure S4F through S4G).

To determine differential regulation of signaling pathways altered in the presence of TPM1-L185F, we utilized label-free DIA-MS whole-proteome analysis (Figure 1B through 1G). Between HD (WT) control and DCM patient–specific iPSC-CMs, 1206 proteins were found to be upregulated and 1357 proteins to be downregulated (Figure 1B). Differentially expressed protein profiles for HD (WT) control and DCM iPSC-CM groups are shown in a Venn diagram (Figure 1C). Principal component analysis (PCA) demonstrated distinct segregation of DCM and WT groups (Figure 1D). Proteomic profiling revealed differential expression of 2563 proteins between WT control and DCM iPSC-CMs (Figure 1E). Using protein enrichment assessment and signaling pathway mapping, we found among the top 15 changed pathways mitochondrial dysfunction and, interestingly, CME (Figure 1F). This prompted us to investigate the molecular mechanisms underlying endocytosis in the presence of DCM mutations such as *TPM1-L185F* in more detail. Of note, our subsequent bioinformatic analysis revealed differentially regulated protein expression profiles in the signaling pathways controlling actin cytoskeleton functions, CME, as well as iron homeostasis in DCM iPSC-CMs (Figure 1G). To validate these findings, protein expression levels of key proteins involved in the CME pathway were quantified via independent methods. Employing 3 independent batches of iPSC cardiac differentiations, we found a downregulation of APOA1 (apolipoprotein AI) in DCM patient–derived iPSC-CMs versus WT controls in immunoblot analysis (Figure S3L through S3M), which is consistent with the proteomics data derived by DIA-MS (Figure 1C through 1G). Moreover, we employed another quantitative method, in-cell-western, reported earlier[50] to confirm the differential expression of proteins of the CME pathway as detected previously by DIA-MS. We confirmed a upregulation of

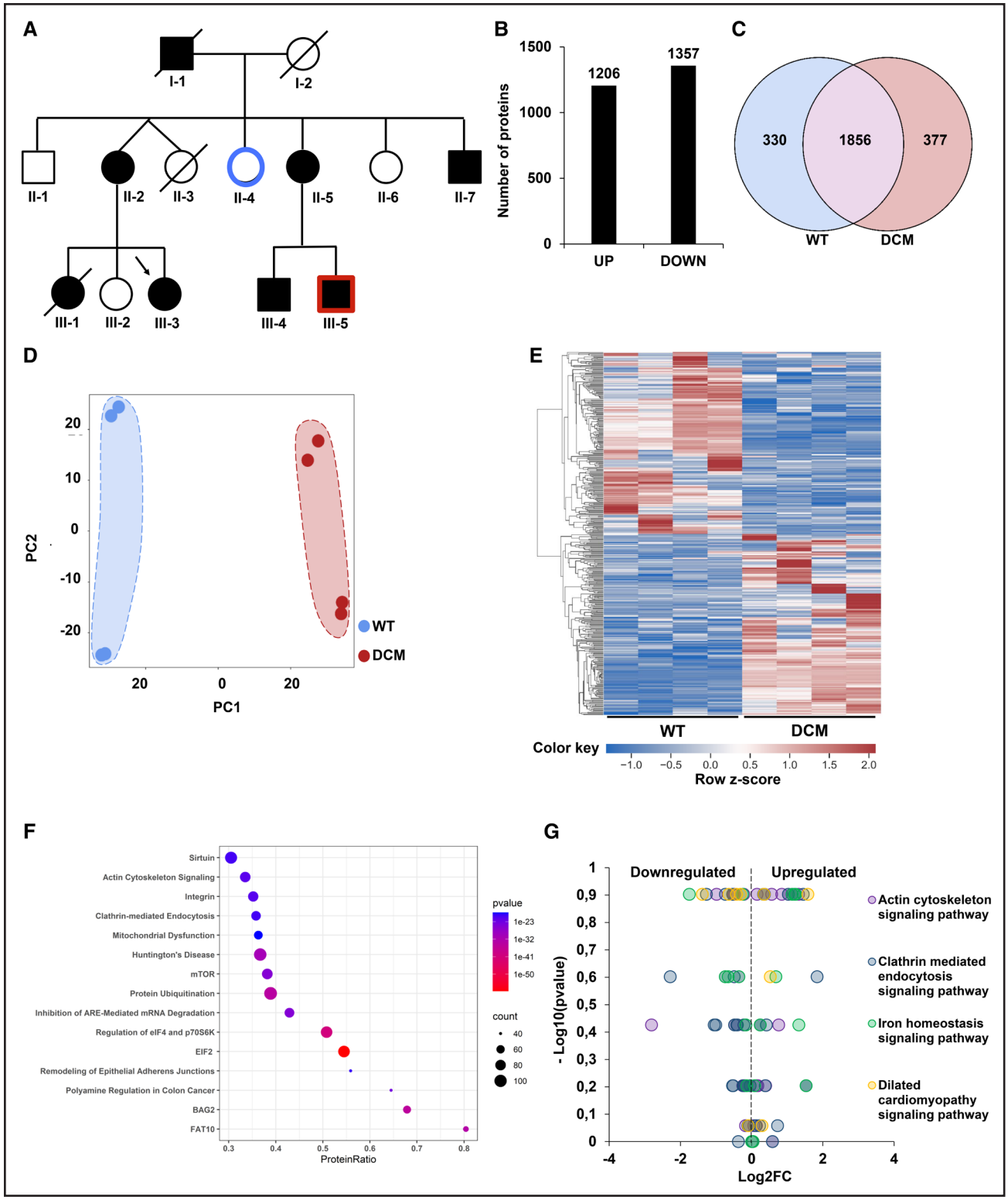

Figure 1. TPM1 (tropomyosin 1)-L185F causes defective contractility and force generation in dilated cardiomyopathy (DCM) patient–specific induced pluripotent stem cell–derived cardiomyocytes (iPSC-CMs).
A, Pedigree of the family carrying the DCM-associated variant *TPM1-L185F* variant. Human iPSCs were generated for 4 mutation carriers and 4 healthy donors. Squares, male and circles, female gender; filled symbols, affected; cross bars, deceased individuals; arrow, proband. Ages at time of diagnosis and last follow-up for gene carriers and age at evaluation for genotype negative control are shown. The healthy donor, individual II-4 (L185F$^{-/-}$, 55 years*) as well as patient III-5 (L185F±, [HTx (heart transplantation)]/27 years*) analyzed in this study are indicated (blue and red, respectively). *Age at first and last evaluation, death, or heart transplantation. **B**, Whole-proteome analysis by label-free DIA-MS (mass spectrometry data-independent acquisition) was used to analyze differently expressed proteins in healthy control iPSC-CMs (*Continued*)

the CME pathway proteins, AP1B1 (adaptor related protein complex 1 subunit beta 1) and DNML1 (dynamin-like protein 1), in DCM (MUT) iPSC-CMs, compared with WT controls (Figure S3N and S3O), in line with our results from the DIA-MS analysis (Figure 1C through 1G). A strong intraindividual and experimental variation was observed in the human iPSC-based model system.[51]

To assess the molecular dysfunctions in endocytosis and iron homeostasis in the presence of the DCM mutation *TPM1-L185F* in more detail, we generated mutation-introduced iPSCs. Isogenic iPSC lines with genetically identical background present substantial advantages for assessing genotype-phenotype relationships in human model systems. We used CRISPR-Cas9 gene editing to introduce the *TPM1-L185F* mutation into WT iPSCs, producing an isogenic MUT-introduced iPSC line (MUT-int/MUT-int; Figure 2A). MUT-int/MUT-int iPSCs express regular levels of pluripotency markers (Figure S2A to S2E) and following cardiac differentiation, regular expression of cardiac markers (Figure S3A through S3K). Like DCM TPM1-L185F patient–derived iPSC-CMs, the isogenic mutation-introduced iPSC-CMs displayed reduced sarcomere length, beating force, and contractility, as well as field potential duration and amplitude, compared with HD control (WT/WT) iPSC-CMs (Figure 2B through 2E; Figure S4A through S4G).

Disrupted sarcomere organization is a key phenotype in presence of DCM mutations.[23,52,53] We tested if impaired sarcomere regularity in presence of TPM1-L185F interrupted sarcomere interactions with the PM via vinculin, a PM-associated protein critical for normal cardiac function.[54–56] Vinculin is known to interact with SAA (sarcomeric alpha-actinin) at the sarcomeres and mediates a connection to F-actin–organizing hubs at the PM.[57–59] We performed immunoprecipitation of SAA and vinculin using WT/MUT, MUT-int/MUT-int versus WT/WT iPSC-CMs and Igg as a negative control (Figure 2F through 2P, Figure S5A through S5C). In presence of TPM1-L185F, we identified a reduced interaction of SAA and vinculin (Figure 2F through 2H) as well as disturbance of additional sarcomere-PM interactions, such as vinculin-TPM and vinculin-TnT (Figure 2F through 2P; Figure S5B through S5I). To further confirm the immunoprecipitation results indicating a reduced interaction of vinculin with TnT, we performed the IP vice-versa and incubated beads decorated with anti-TnT antibody with cell lysates from WT (healthy control) and MUT (DCM patient–specific TnT-R173W iPSC-CMs) groups. Next, eluted fractions were subjected to nanoliquid chromatography/liquid chromatography MS-based analysis. Results show that TnT interacts with vinculin in the WT group, as well as a reduced interaction of TnT and vinculin in the DCM (MUT) group (Figure S5J and S5K; Table S1). Negative controls included a no-antibody-control as well as iPSC-CMs from a CRISPR/Cas9–edited TnT knockout iPSC-CM line[23] (Figure S5J and S5K; Table S1). Together, these findings support that interactions of sarcomere proteins such as TnT with vinculin are impaired in iPSC-CMs carrying mutations in sarcomere proteins. To further confirm disrupted sarcomere-PM interactions in presence of different DCM mutations, we employed CRISPR/Cas9 generated, mutation-introduced iPSC-CMs carrying the DCM mutation *TnT-R141W* (*MUT2-int/MUT2-int*) described earlier.[26] We established reduced colocalization of vinculin and sarcomeric TnT (Figure 2Q through 2R) in patient-specific iPSC-CMs (WT/MUT) and mutation-introduced iPSC-CMs carrying *TPM1-L185F* (*MUT1-int/MUT1-int*) or *TnT-R141W* (*MUT2-int/MUT2-int*) as well as isogenic WT controls (WT/WT). Taken together, our data demonstrate that in presence of 2 different DCM mutations, *TPM1-L185F* and *TnT-R141W*, sarcomere interactions with the PM are disrupted.

Impaired F-Actin Polymerization Is Linked to Defective CME and Endosome Distribution in Presence of DCM Mutations

We speculated that disrupted vinculin interactions in DCM iPSC-CMs might be accompanied by dysfunction of the vinculin/F-actin interface, a major hub for

Figure 1 Continued. (WT/WT; WT [wild type]) vs DCM patient–derived iPSC-CMs (WT/MUT [mutation]; patient). 1206 proteins were found to be upregulated with a threshold of log2(foldchange [FC] [WT/DCM]) > 0. Moreover, 1357 proteins were found to be downregulated with a threshold of log2(FC [WT/DCM])<0. **C**, Venn diagram of differentially expressed protein profiles for healthy donor (WT control) and DCM iPSC-CM groups. To identify commonly expressed proteins, a cutoff for the *P* value (0.05) was used. 1856 proteins were found commonly expressed in both groups with a *P*>0.05. Three hundred thirty proteins were found highly expressed in the WT iPSC-CM group with a threshold of log2(FC [WT/DCM]>0, and 377 proteins were highly expressed in the DCM iPSC-CM group with a threshold of log2(FC [WT/DCM]<0; for both groups, all *P* values were <0.05. **D**, Principal component analysis for proteomic expression profiling detected for WT control and DCM iPSC-CMs. **E**, Heatmap of proteomic profiling for WT control and DCM iPSC-CMs (n=4 replicates each). Cluster analysis was performed for 2563 proteins (rows) via Euclidean distance assessment by clustermap (Seaborn). Four hundred forty-five proteins were found when applying a threshold of log2(FC [WT/DCM]) >1 and <−1 to filter for proteins that were highly expressed in WT or DCM groups. **F**, A dot plot for the top 15 changed pathways between WT control and DCM iPSC-CMs is shown. Pathways were ranked according to protein ratios, represented by dots color-coded according to the *P* values. The size of the dots corresponds to the number of proteins that were differently expressed between WT control and DCM iPSC-CMs. Pathways were retrieved using ingenuity pathway analysis. **G**, Volcano plot showing upregulated vs downregulated protein expression profiles in the signaling pathways for actin cytoskeleton (purple), clathrin-mediated endocytosis (blue), iron homeostasis (green), as well as the DCM signaling pathway (yellow) between WT (healthy donor) and DCM groups. A nonparametric, Wilcoxon signed-rank test was employed to establish statistical significance. AT10 indicates human leukocyte antigen-F adjacent transcript 10; BAG2, Bcl2-associated athanogene 2; ELF2, ETS transcription factor 2; eLF4, ETS transcription factor 4; mTOR, mammalian target of rapamycin; and PC, principal component.

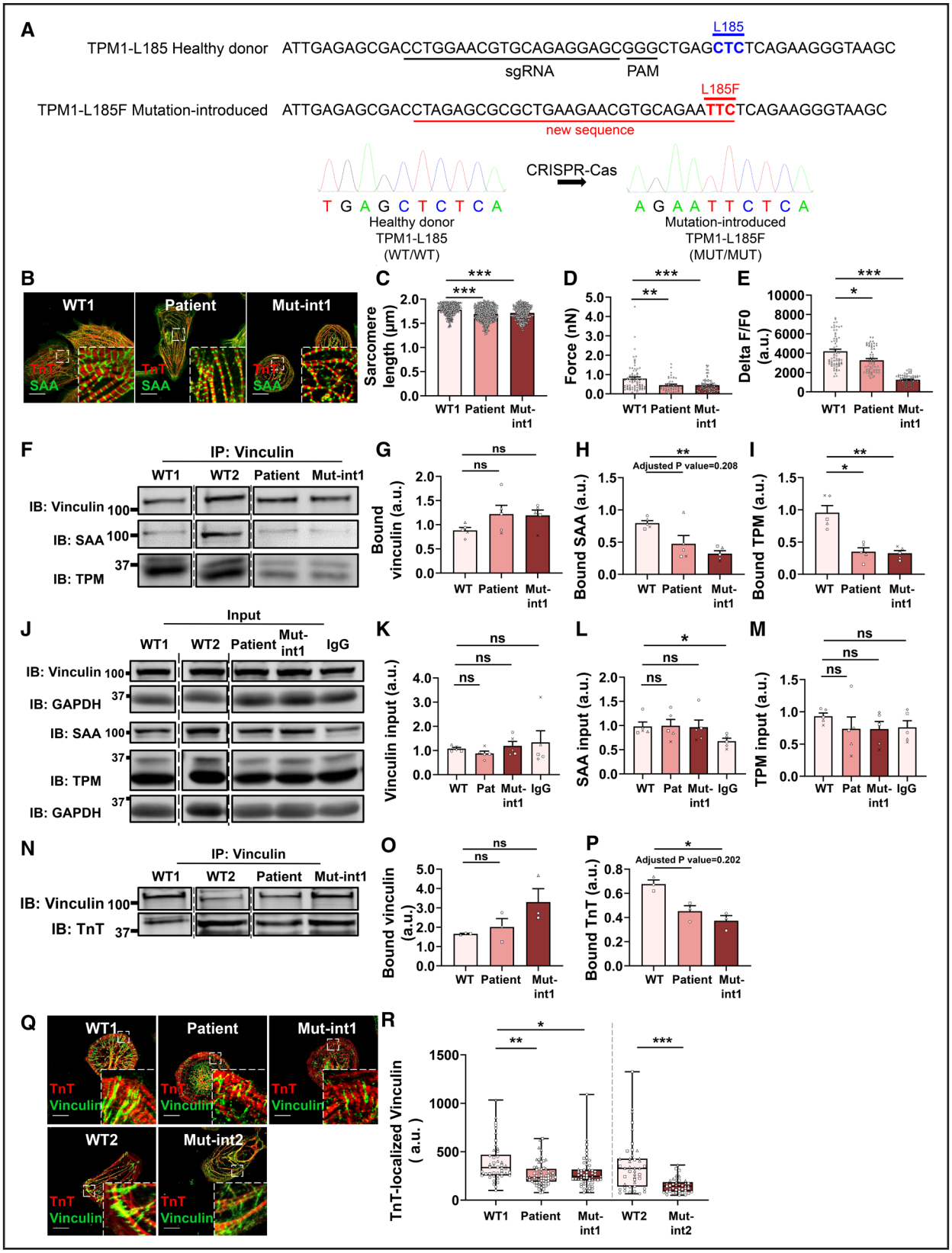

Figure 2. TPM1 (tropomyosin 1)-L185F disrupts sarcomere connections with plasma membrane microdomains in dilated cardiomyopathy (DCM) patient–specific induced pluripotent stem cell–derived cardiomyocytes (iPSC-CMs).
A, CRISPR-Cas genome editing to generate *TPM1-L185F* mutation-introduced (MUT-int1) iPSCs. **B** and **C**, Reduced sarcomere length in patient and MUT-int/MUT-int1 compared with WT iPSC-CMs. **B**, Representative images from cells stained with TnT (troponin T) and SAA (sarcomeric alpha-actinin) antibodies. Scale bar, 20 μm. Enlarged regions were zoomed in 5×. **C**, Quantification of **B**. ***$P<0.001$ for (*Continued*)

organization of F-actin filaments and PIP2-enriched microdomains at the PM. To test if actin microfilament polymerization was altered, we measured the ratio of polymerized F-actin and monomeric G-actin (globular actin). In DCM iPSC-CMs (patient-specific WT/MUT and Cas9-mutation-introduced MUT-int/MUT-int), reduced F/G-actin ratios were detected, compared with WT/WT controls (Figure 3A), whereas total beta-actin protein levels were not changed between the groups (Figure S6A). As PIP2-enriched microdomains at the PM are critical for actin polymerization,[60–62] we quantified PIP2 levels in the presence of the 2 DCM mutations, *TPM1-L185F* and *TnT-R141W*. DCM patient–specific and Cas9-mutation-introduced iPSC-CMs contained a reduced amount of PM-localized PIP2, compared with WT/WT iPSC-CMs (Figure 3B and 3C). To confirm our findings, we next sought to introduce the molecular phenotype observed in DCM iPSC-CMs, reduced PIP2 levels, into WT/WT iPSC-CMs. We utilized chemical inhibition of PIP5K (phosphatidylinositol-4-phosphate 5-kinase), a major PIP2 synthesizing enzyme at the PM,[63] via UNC3230, a PIP5K-specific inhibitor.[64] UNC3230-treated WT/WT iPSC-CMs showed reduced PIP2 levels at the PM (Figure S6B and S6C). As expected, UNC3230 treatment resulted also in reduced F-actin levels in WT/WT iPSC-CMs (Figure S6D and S6E), thereby recapitulating the molecular phenotype observed in DCM iPSC-CMs. These findings demonstrated decreased actin polymerization and PM-localized PIP2 levels in DCM patient–specific and Cas9 mutation-introduced iPSC-CMs. This is yet more relevant as a main route for cellular cargo import, CME, is regulated at actin-assembling PM hubs controlling PIP2 synthesis and turnover.[65–67] In cardiomyocytes, critical cargo such as iron (Fe III+) is internalized via the transferrin receptor by CME and distributed by endosomes.[34] Considering the importance of PIP2-mediated F-actin assembly for CME, we assessed if CME-dependent cargo uptake was altered in the presence of DCM mutations. We examined continuous uptake of transferrin-bound iron in live iPSC-CMs and observed a reduction of CME-based transferrin uptake in DCM patient–specific and Cas9-mutation-introduced iPSC-CMs (Figure 3D and 3E; Figure S6F) while expression levels of the transferrin receptor were not significantly changed between groups (Figure S6G). To exclude the possibility that the observed reduction of CME-dependent cargo uptake was limited to the transferrin receptor, we analyzed internalization of LDL (low-density lipoprotein) via the LDL receptor, which was also reduced in DCM iPSC-CMs (Figure S7A and S7B). LDL receptor expression levels were not significantly altered between groups (Figure S7C). Next, we tested whether a different cellular uptake

Figure 2 Continued. WT1 vs patient (Pat; adjusted $P<1\times10^{-15}$) and WT1 vs Mut-int1 (adjusted $P=1.56\times10^{-9}$; Kruskal-Wallis test and Dunn multiple comparisons test). **D**, Reduced beating force in WT/MUT and *TPM1-L185F* MUT-introduced iPSC-CMs. $^{**}P<0.01$ for WT1 vs Pat (adjusted $P=1.35\times10^{-3}$); $^{***}P<0.001$ for WT1 vs Mut-int1 (adjusted $P=1.36\times10^{-4}$; Kruskal-Wallis test and Dunn multiple comparisons test). **E**, WT/MUT and *TPM1-L185F* MUT-introduced iPSC-CMs display impaired contractility indicated by reduced delta F/F0. $^{*}P<0.05$ for WT1 vs patient (Pat; adjusted $P=2.65\times10^{-2}$); $^{***}P<0.001$ for WT1 vs Mut-int1 (adjusted $P<1\times10^{-15}$; Kruskal-Wallis test and Dunn multiple comparisons test). **F** through **I**, In presence of TPM1-L185F, a lower amount of SAA (ACTN2) and TPM (TPM1) bind to vinculin. **F**, Representative images of immunoblot membranes were shown. **G**, No significant difference was observed in the amount of vinculin bound with beads. Ns for WT vs Pat and WT vs Mut-int1 (Kruskal-Wallis test and Dunn multiple comparisons test). **H**, Reduced binding of SAA to vinculin in presence of TPM1-L185F. Data were normalized by bound vinculin from corresponding groups, respectively. ns, not significant (adjusted $P=0.208$) for WT vs Pat; $^{*}P<0.05$ WT vs Mut-int1 (adjusted $P=0.0178$; Kruskal-Wallis test and Dunn multiple comparisons test). **I**, Reduced binding of TPM to vinculin in presence of TPM1-L185F. Data were normalized by bound vinculin from corresponding groups, respectively. $^{*}P<0.05$ for WT vs Pat (adjusted $P=0.0267$) and $^{**}P<0.01$ for WT vs MUT-int1 (adjusted $P=9.36\times10^{-3}$; Kruskal-Wallis test and Dunn multiple comparisons test). Data were normalized by WT (WT1, WT2). **J** through **M**, The protein levels of vinculin (**K**), SAA (**L**), and TPM (**M**) were not significantly different in DCM patient–derived (Pat, WT/MUT) and *TPM1-L185F* mutation-introduced iPSC-CMs (Mut-int1, MUT-int1/MUT-int) compared to WT group in input fractions. **J**, Representative membrane scans of membranes from input samples. **K**, Not significant (ns) for WT vs patient, WT vs Mut-int1 iPSC-CMs, and WT vs IgG (Kruskal-Wallis test and Dunn multiple comparisons test). **L**, ns, not significant for WT vs patient and WT vs Mut-int1. $^{*}P<0.05$ (adjusted $P=0.0418$) for WT vs IgG (Kruskal-Wallis test and Dunn multiple comparisons test). **M**, NS for WT vs patient, WT vs Mut-int1, and WT vs IgG (Kruskal-Wallis test and Dunn multiple comparisons test). Data were normalized by GAPDH. **N** through **P**, Reduced binding of TnT to vinculin in presence of TPM1-L185F. **N**, Representative images of immunoblot membranes. **O**, The amount of vinculin bound to anti-vinculin antibody decorated beads was comparable between groups. ns, not significant for WT vs Pat and WT vs Mut-int1 (Kruskal-Wallis test and Dunn multiple comparisons test). Per group, n=3 experiments (n=1 independent cardiac differentiation). **P**, Reduced binding of TnT to vinculin is observed in presence of the DCM mutation TPM1-L185F. Signal corresponding to bound TnT is normalized for the corresponding amount of bound vinculin by dividing the signal for bound TnT by the signal for bound vinculin in the respective groups. Bar graph shows normalized signal intensities. ns, not significant (adjusted $P=0.202$) for WT vs Pat; $^{*}P<0.05$ for WT vs MUT-int1 (adjusted $P=0.0341$; Kruskal-Wallis test and Dunn multiple comparisons test). Data were normalized by WT (WT1, WT2). Per group, n=3 experiments (n=1 independent cardiac differentiation). **Q** through **R**, Reduced amount of TnT-localized vinculin localized in presence of mutations in sarcomere proteins, TPM1-L185F (Mut-int1) and TnT-R141W (Mut-int2). **Q**, Representative confocal images following immunostaining for vinculin and TnT; scale bar, 20 µm. Enlarged regions were zoomed in 5×. **R**, Quantification of **Q**. $^{**}P<0.01$ for WT1 vs Pat (adjusted $P=3.58\times10^{-3}$); $^{*}P<0.05$ for WT1 vs MUT-int1 (adjusted $P=0.0122$); $^{***}P<0.001$ for WT2 vs MUT-int2 (adjusted $P=8.47\times10^{-8}$; Kruskal-Wallis test and Dunn multiple comparisons test). Data are shown as mean±SEM. Images shown in figures are representative of the average value of each group. Unless indicated otherwise, the number of independent experiments equals the number of independent iPSC cardiac differentiations. Data points per experiment are shown as different shapes: # 1 as circles, #2 as triangles, #3 as squares, #4 as diamonds, #5 as crosses. Au indicates arbitrary unit; IB, immunoblot; Mut-int, mutation-introduced; PAM, protospacer adjacent motif; Pat, patient; sgRNA, single guide RNA; and WT, wild type.

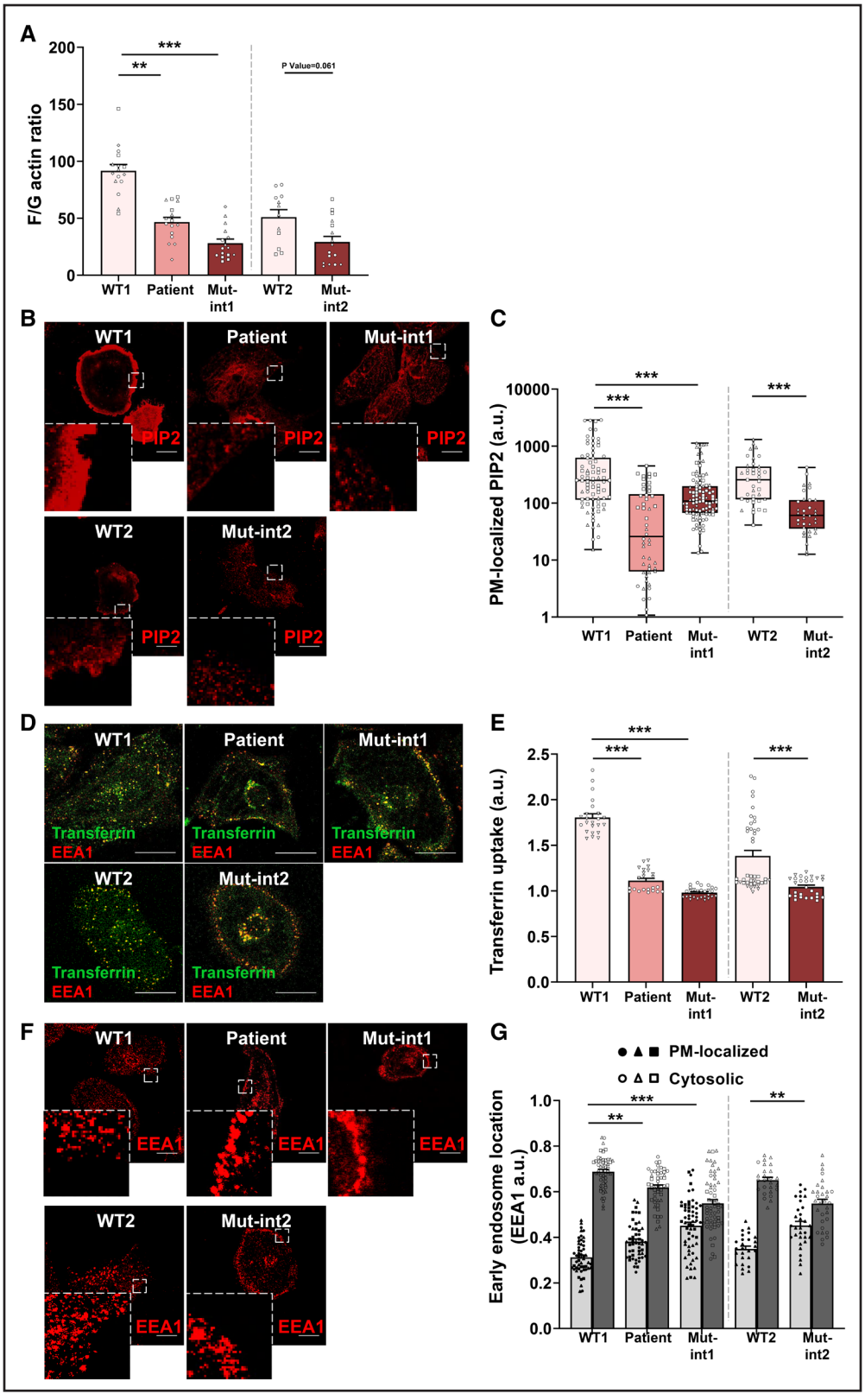

Figure 3. Impaired fibrous actin (F-actin) polymerization is linked to defective clathrin-mediated endocytosis and endosome distribution in presence of dilated cardiomyopathy (DCM) mutations.

A, Reduced F-actin content in WT (wild type)/MUT (mutation) and mutation-introduced (Mut-int1)/MUT-int induced pluripotent stem cell–derived cardiomyocytes (iPSC-CMs). Actin polymerization was measured via detection of phalloidin (F-actin) and DNase I (G-actin [globular actin]) immunostaining using a high-content plate reader. DAPI (4′,6-diamidino-2-phenylindole) was used to normalize total cell numbers. $^{**}P<0.01$ for WT1 vs Pat (adjusted $P=1.25\times10^{-3}$); $^{***}P<0.001$ for WT1 vs MUT-int1 (adjusted $P=4.77\times10^{-8}$); ns. for WT2 vs MUT-int2 (adjusted $P=0.061$; (*Continued*)

process involving polymerized actin filaments and lipids at the PM, phagocytosis, would be affected by DCM mutations in sarcomere proteins. We reasoned that in phagocytosis, cytoskeleton, and PM lipids work in a coordinated manner for uptake of large particles[68]; thus this process might be altered in DCM iPSC-CMs which display a defective PM actin polymerization and lipid organization. Measurements of phagocytosis in live iPSC-CMs revealed reduced phagocytosis in DCM iPSC-CMs (Figure S7D). This indicated that disrupted actin polymerization and impaired lipid composition at the PM in presence of DCM mutations result in critical defects of cellular cargo uptake processes, such as CME and phagocytosis. This was further supported by the differential expression of proteins involved in phagocytosis pathways observed in DCM iPSC-CMs compared to WT control (Figure S7E and S7F). Next, we tested if endosome-dependent distribution of CME-internalized cargo, such as transferrin-bound iron, was altered in iPSC-CMs carrying DCM mutations. To first test if endosome distribution is affected by impaired actin polymerization, spatial localization of endosomes was tracked using the early endosome (EE) marker EEA1 (early endosome antigen 1). While in WT iPSC-CMs, EE cargo carriers were evenly distributed throughout the cells, no regular distribution of EEs was observed in DCM iPSC-CMs (patient-specific WT/MUT and Cas9-edited MUT-int/MUT-int). Instead, in the presence of DCM mutations, cargo-carrying EEs arrested at the PM (Figure 3F and 3G; Figure S7G). Moreover, this new DCM disease phenotype, defective distribution of cargo-carrying EEs, could be successfully introduced into WT iPSC-CMs via a potent inhibitor of actin polymerization, Lat-A (latrunculin A). Lat-A treatment resulted in a reduced F/G-actin ratio (Figure S8A) as well as accumulation of EEs at the PM in WT iPSC-CMs (Figure S8B and S8C), thereby phenocopying the presentation of DCM iPSC-CMs (Figure 3F and 3G). Our data demonstrate defective cargo uptake and distribution in DCM patient–specific iPSC-CMs as well as isogenic controls carrying 2 different DCM mutations, *TPM1-L185F* and *TnT-R141W*.

Iron Deficiency in the Presence of DCM Mutations Causes Mitochondrial Dysfunction and Reduced Contractility in DCM iPSC-CMs

Mitochondria, major recipient of iron (Fe) in the cell[34,69] require Fe for electron transport in the mitochondrial respiratory chain as well as oxygen transport.[70] Iron imbalance specifically in the mitochondria is deleterious as its critical functions require a fine balance of mitochondrial iron.[34] Iron deficiency has been associated with cardiovascular disease and HF.[5] Therefore, we assessed the effects of impaired uptake of transferrin-bound iron and impaired EE distribution on mitochondrial function. We examined Fe levels in mitochondria in live cells and found that the mitochondria of DCM iPSC-CMs (patient-specific WT/MUT and Cas9-mutation-introduced MUT-int/MUT-int) displayed depleted iron levels, compared to control (Figure 4A and B). This was true for both DCM mutations, *TPM1-L185F* and *TnT-R141W* (Figure 4A and B) and was accompanied by a reduction of mitochondrial membrane potential, supporting reduced function of iron-deficient mitochondria in DCM iPSC-CMs (Figure S9A and S9B). Mitochondria are major sites of intracellular iron consumption, due to their Fe/S clusters and heme groups which are essential for the function of electron transport chain complexes I to IV.[71] In cardiomyocytes, mitochondria provide fuel for processes that demand high levels of energy, such as contractility. Thus, depleted mitochondrial iron levels in cardiomyocytes are detrimental and contribute to defective mitochondrial respiration as well as impaired contractility in cardiomyocytes, as shown previously.[72] To measure mitochondrial respiratory activity, a Seahorse XF analyzer assay was employed and revealed the basal oxygen consumption rate of mitochondrial respiration to be reduced in presence of DCM mutations (Figure 4C and 4D; Figure S9C and S9D), indicating impaired mitochondrial function in DCM iPSC-CMs.

Clinical trials demonstrated increased iron supply in iron-deficient HF patients to be beneficial for cardiac function.[8] Here, we show that in presence of DCM mutations in sarcomere proteins, iPSC-CMs fail to perform normal CME-dependent uptake of transferrin-bound iron via the

Figure 3 Continued. Kruskal-Wallis test and Dunn multiple comparisons test). **B** and **C**, Reduced phosphatidylinositol 4,5-bisphosphate (PIP2) levels on the plasma membrane (PM) in WT/MUT and MUT-int/MUT-int iPSC-CMs. **B**, Representative confocal images following PIP2-specific immunostaining. Scale bar, 20 µm. Enlarged regions were zoomed in 6×. **C**, Quantification of **B**. ***P<0.001 for WT1 vs Pat (adjusted P=4.23×10^{-12}), WT1 vs Mut-int1 (adjusted P=1.23×10^{-4}), and WT2 vs Mut-int2 (adjusted P=6.92×10^{-7}; Kruskal-Wallis test and Dunn multiple comparisons test). **D** and **E**, Impaired transferrin uptake in WT/MUT and MUT-int/MUT-int iPSC-CMs. **D**, Representative ×63 confocal images of continuous transferrin uptake at 5 minutes. Scale bar, 20 µm. **E**, Quantification of ×20 confocal Z stack images of continuous transferrin uptake at 5 minutes normalized by uptake at 0 minute. ***P<0.001 for WT1 vs Pat (adjusted P=2×10^{-15}), WT1 vs Mut-int1 (adjusted P=5.88×10^{-6}), and WT2 vs Mut-int2 (adjusted P=2.24×10^{-4}; Kruskal-Wallis test and Dunn multiple comparisons test). **F** and **G**, Abnormal early endosome distribution in WT/MUT and MUT-int/MUT-int iPSC-CMs. **F**, Representative ×63 confocal images. Scale bar, 20 µm. Enlarged regions were zoomed in ×6.5. **G**, Quantification of confocal images following immunostaining with an anti-EEA1 antibody; scale bar, 20 µm. **P<0.01 for WT1 vs Pat (adjusted P=1.347×10^{-3}); ***P<0.001 forWT1 vs MUT-int1 (adjusted P=8.16×10^{-11}); **P<0.01 for WT2 vs MUT-int2 (adjusted P=1.105×10^{-3}; Kruskal-Wallis test and Dunn multiple comparisons test). Data are shown as mean±SEM. Images shown in figures are representative of the average value of each group. Unless indicated otherwise, the number of independent experiments equals the number of independent iPSC cardiac differentiations. Data points per experiment are shown as different shapes: # 1 as circles, #2 as triangles, #3 as squares, #4 as diamonds, #5 as crosses. Au indicates arbitrary unit; EEA1, early endosome antigen 1; and F/G actin, fibrous/globular actin.

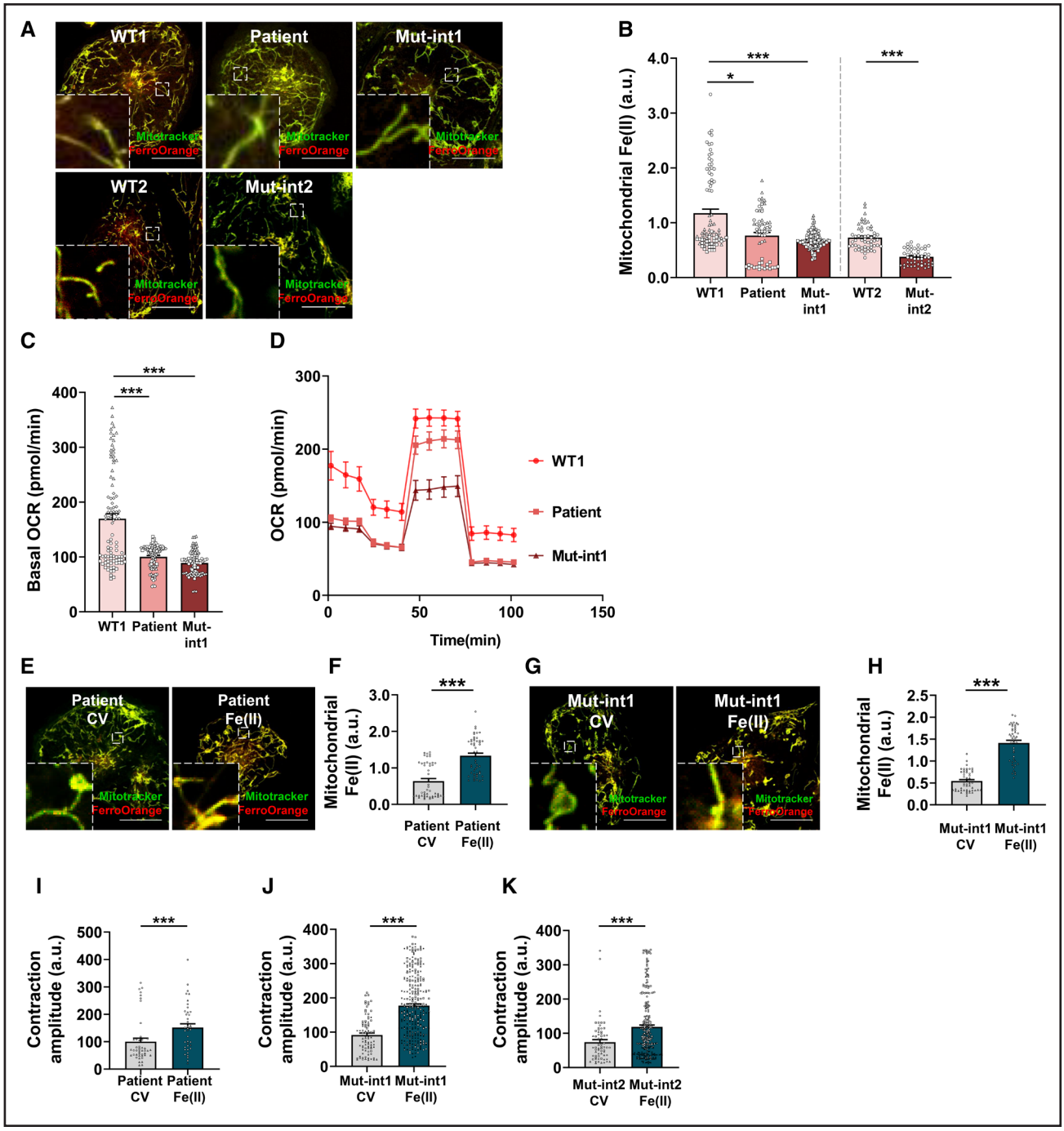

Figure 4. Iron deficiency in the presence of dilated cardiomyopathy (DCM) mutations causes mitochondrial dysfunction and reduced contractility in DCM induced pluripotent stem cell–derived cardiomyocytes (iPSC-CMs).
A and **B**, Mitochondrial Fe (II) levels are reduced in WT (wild type)/MUT (mutation) and mutation-introduced (Mut-int1)/MUT-int iPSC-CMs. Representative ×63 confocal images (**A**) and region of interest (ROI)–based quantification (**B**) following Mitotracker and FerroOrange labeling. Scale bar, 20 μm. Enlarged regions were zoomed in ×5.8. *P<0.05 for WT1 vs patient (Pat; adjusted P=1.86×10^{-2}); ***P<0.001 for WT1 vs Mut-int1 (adjusted P=9.88×10^{-6}) and WT2 vs Mut-int2 (adjusted P=2.15×10^{-10}; Kruskal-Wallis test and Dunn multiple comparisons test). **C** and **D**, In presence of DCM mutations, iPSC-CMs display reduced basal oxygen consumption rate (OCR, pmol/min). **C**, DCM patient–derived and Mut-int1 iPSC-CMs showed defective mitochondrial respiration. **D**, A complete diagram of mitochondrial respiration recorded via a Seahorse XF analyzer is shown. ***P<0.001 for WT1 vs patient (adjusted P=8.17×10^{-6}) and WT1 vs mut-int1 (adjusted P=1×10^{-15}) iPSC-CMs. Kruskal-Wallis test and Dunn multiple comparisons test. **E** through **H**, Fe(II) treatment can replenish mitochondrial Fe levels in patient (WT/MUT) and *TPM1 (tropomyosin 1)-L185F* mutation–introduced iPSC-CMs (Mut-int1). Representative ×63 confocal images (**E** and **G**) and quantification (**F** and **H**) of live cells labeled with Mitotracker and FerroOrange following CV or ammonium Fe (II) sulfate (100 μM, 30 minutes) treatment; scale bar, 20 μm. Enlarged regions were zoomed in 6.3×. ***P<0.001 for CV vs Fe(II) patient (P=1.65×10^{-8}) and CV vs Fe(II) Mut-int1 (P<1×10^{-15}) iPSC-CMs (Mann-Whitney U test). **I** through **K**, Fe (II) treatment rescued the contraction amplitude in WT/MUT and MUT-int/MUT-int iPSC-CMs. Contractility was measured via video-based motion-traction analysis. ***P<0.001 for control vehicle (CV) vs Fe (II) in DCM patient (Pat) iPSC-CMs (*Continued*)

transferrin receptor. We thus confirmed that iron supplementation recovered the reduced mitochondrial iron levels in DCM iPSC-CMs (patient-specific WT/MUT and Cas9-engineered MUT-int/MUT-int; Figure 4E through 4H). Importantly, replenishing iron levels also rescued impaired contractility in DCM patient–specific iPSC-CMs (WT/MUT) as well as in 2 Cas9-mutation–introduced iPSC-CM lines carrying 2 different DCM mutations, *TPM1-L185F* and *TnT-R141W* (Figure 4I through 4K). Together, these findings indicated that increased mitochondrial iron levels resulted in improved contractility in DCM iPSC-CMs. However, as sarcomere dysfunction due to DCM mutations represents a serious pathological disruption, the improved mitochondrial iron levels in presence of iron treatment could only deliver a partial rescue of contractility in DCM iPSC-CMs.

We next performed control experiments testing the contribution of DMT1 (divalent metal transporter 1)-based iron uptake into iPSC-CMs. While CME-based uptake of transferrin-bound iron in its ferric form, Fe(III), covers the majority of intracellular iron demand, DMT1 enables efficient uptake of nontransferrin-bound iron, such as the ferro form, Fe(II).[73] We first measured CME-based uptake of transferrin-bound iron via the transferrin receptor in presence of ferro iron, Fe(II), supplementation and confirmed that Fe(II) treatment does not increase uptake of transferrin-bound iron, Fe(III), in DCM iPSC-CMs (Mut-int1; Figure S9E and S9F). This indicated that supplemented ferro iron, Fe (II), which enters cells via a CME-independent pathway, does not affect CME in presence of DCM mutations in sarcomere proteins. Moreover, we treated Mut-int1 iPSC-CMs with ebselen, a DMT1 inhibitor,[74] in the presence of ferro iron, Fe (II), supplementation. We measured the uptake of transferrin-bound iron in presence of ebselen and found that ebselen treatment does not affect the CME-based uptake of ferric iron, Fe (III), via transferrin (Figure S9E and S9F). Furthermore, we confirmed that ebselen treatment in presence of Fe (II) supplementation blocked an improvement of mitochondrial iron levels delivered by Fe (II) in Mut-int1 iPSC-CMs (Figure S9G and S9H). This supported that in iPSC-CMs, supplemented ferro iron, Fe (II, is internalized via DMT1 to deliver intracellular recovery of iron levels in the mitochondria. Consistently, ebselen treatment in presence of Fe (II) supplementation prevented an improvement of contractility delivered by Fe(II; Figure S9I). This further corroborated that internalization of ferro iron, Fe (II), into iPSC-CMs occurs via DMT1. This process occurs independent of CME, as Fe(II) treatment did not alter transferrin uptake (Figure S9E and S9F) nor internalization of another CME-dependent cargo, LDL (Figure S9J and S9K). Moreover, DMT1-dependent uptake of ferro iron, Fe (II), into iPSC-CMs did not alter a different cargo internalization process, phagocytosis, in Mut-int1 iPSC-CMs (Figure S9L). To confirm that iron deficiency due to impaired endocytosis and endosome distribution is linked to actin polymerization defects in the presence of DCM mutations, we quantified Fe levels of Lat-A–treated WT iPSC-CMs. Our data show that Lat-A–induced actin polymerization defects can introduce an imbalance of iron levels into WT control iPSC-CMs (Figure S9M) which could be recovered by subsequent iron supplementation (Figure S9M).

Fe deficiency has been associated with increased production of reactive oxygen species in HF.[75] To test if this molecular disease phenotype is recapitulated in DCM iPSC-CMs, we measured total reactive oxygen species levels in live iPSC-CMs. As expected, we observed elevated mitochondrial superoxide levels in DCM iPSC-CMs (WT/MUT and MUT1-int/MUT1-int; Figure S9N) which could be rescued by Fe supplementation (Figure S9O and S9P). This confirmed that Fe deficiency may contribute to elevated reactive oxygen species levels in particular in the mitochondria of DCM iPSC-CMs.

To further corroborate the contribution of the newly described CME-dependent signaling pathway to the observed molecular pathophenotypes, such as reduced mitochondrial activity, we performed chemical phenotype-introduce experiments. We applied small molecule-based treatment with UNC3230, inhibiting PI4P5K-dependent PIP2 production at the PM, a critical step required for initiation of CME. UNC3230 treatment reduced basal mitochondrial respiration in WT1 iPSC-CMs, compared with control vehicle (Figure S9Q and S9R). Likewise, we found upon treatment of WT1 iPSC-CMs with Lat-A, which blocks actin polymerization necessary for CME induction, a decrease of basal mitochondrial respiration (Figure S9S and S9T).

Together, our results indicated mitochondrial iron levels as well as impaired mitochondrial respiration in DCM iPSC-CMs as a consequence of defective actin polymerization, impaired endocytosis of CME-dependent cargo, as well as defective intracellular endosome-dependent cargo distribution. These molecular causes of iron deficiency exacerbate the defective contractility due to sarcomere dysfunction in DCM iPSC-CMs.

Recovering Actin Polymerization via RhoA Activation Rescues PM-Localized PIP2 Levels and Uptake of Transferrin-Bound Iron

To rescue the molecular DCM disease phenotypes resulting in mitochondrial iron deficiency in DCM iPSC-CMs,

Figure 4 Continued. (P=8.80×10^{-4}), CV vs Fe(II) in Mut-int1 iPSC-CMs (P<1×10^{-15}) and CV vs Fe(II) Mut-int2 (P=1.60×10^{-4}), calculated by Mann-Whitney *U* test. Data are shown as mean±SEM. Images shown in figures are representative of the average value of each group. Unless indicated otherwise, the number of independent experiments equals the number of independent iPSC cardiac differentiations. Data points per experiment are shown as different shapes: # 1 as circles, #2 as triangles, #3 as squares, #4 as diamonds, #5 as crosses, #6 as stars. Au indicates arbitrary units.

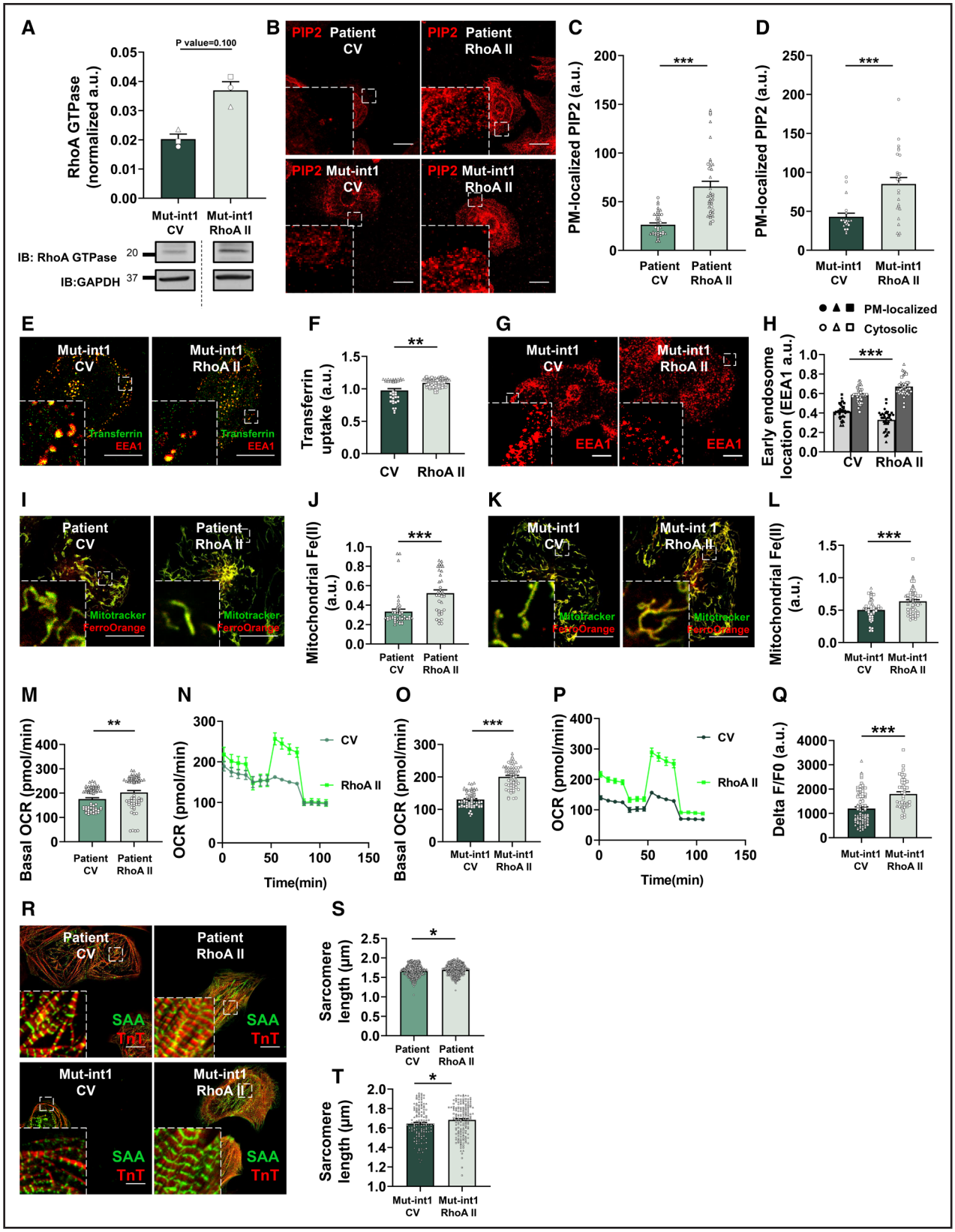

Figure 5. Recovering actin polymerization via RhoA (Ras homolog family member A) activation rescues plasma membrane (PM)-localized phosphatidylinositol 4,5-bisphosphate (PIP2) levels and uptake of transferrin-bound iron.

A, RhoA II (Rho activator II) treatment (3 μg/mL, 16 hours) increases the expression levels of RhoA GTPase in mutation-introduced (Mut-int1) induced pluripotent stem cell–derived cardiomyocytes (iPSC-CMs). ns for CV vs RhoA II (P=0.100; Mann-Whitney U test). **B** through **D**, Increased PIP2 around the PM after Rho activator II treatment in both dilated cardiomyopathy (DCM) patient–derived (Pat) and *TPM1* (*Continued*)

we turned to RhoA (Ras homolog family member A), a Rho GTPase which regulates PIP2 production via PIP5K activation and F-actin polymerization.[76,77] Under chronic stress, loss of RhoA in cardiomyocytes leads to decreased contractility.[78] We applied a RhoA activating peptide, RhoA II (Rho activator II), which has been shown previously to increase PIP2 production in mammalian cells.[79] We established that RhoA II treatment indeed activated the RhoA GTPase in MUT1-int/MUT1-int iPSC-CMs, compared to control vehicle treatment (Figure 5A). Next, we quantified PIP2 levels at the PM following RhoA II treatment. We observed an increase of PM-localized PIP2 in presence of RhoA II, compared to control vehicle, in both DCM patient–specific (WT/MUT) and Cas9-mutation–introduced (MUT-int/MUT-int) iPSC-CMs (Figure 5B through 5D). Moreover, we showed that RhoA II treatment activated actin polymerization in DCM iPSC-CMs (MUT1-int/MUT1-int), compared to control vehicle (Figure S10A). RhoA activation also increased the endocytosis-dependent uptake of transferrin receptor (Figure 5E and 5F) and rescued defective endosome distribution in DCM mutation-introduced iPSC-CMs to the levels observed in WT control (WT/WT) iPSC-CMs (Figure 5G and 5H). Importantly, treatment with RhoA II rescued mitochondrial iron levels in DCM iPSC-CMs (Figure 5I through 5L), mitochondrial respiration (Figure 5M through 5P) as well as sarcomere-PM connections such as the interaction of TnT with vinculin (Figure S10B through S10D). This highlights the critical role PIP2 plays at the sarcomere/F-actin/PM regulatory hub. Consequently, Rho activator II treatment improved contractility in DCM iPSC-CMs, such as amplitude and maximal decay (Figure 5Q; Figure S10E through S10G) and recovered sarcomere protein organization in DCM iPSC-CMs (patient-specific WT/MUT and Cas9-engineered MUT-int/MUT-int; Figure 5R through 5T). Our findings stress the intricate molecular mechanisms controlled by sarcomere interactions with F-actin and PM-localized PIP2 and their dysfunction in DCM iPSC-CMs.

CRISPR/Cas9 Correction of the Patient-Specific DCM Mutation *TPM1-L185F* Rescues Endosome Distribution and Mitochondrial Iron Levels in DCM-Corrected iPSC-CMs

Isogenic cell lines are a valuable tool to ascertain molecular disease mechanisms and genotype-phenotype correlations. To further demonstrate that the DCM mutation *TPM1-L185F* causes defective uptake and distribution of transferrin-bound iron, resulting in mitochondrial iron deficiency and reduced contractility, we corrected the DCM mutation via CRISPR/Cas9 gene editing. We generated an isogenic mutation-corrected (Mut-cor; WT-cor/ WT-cor) iPSC line, using site-specific CRISPR-Cas9 gene editing (Figure 6A; Figure S11A through S11E) and differentiated the Mut-cor iPSCs (WT-cor/WT-cor) into iPSC-CMs (Figure S11F through S11P). First, we confirmed that actin polymerization was recovered in Mut-cor iPSC-CMs (WT-cor/ WT-cor) compared with DCM patient–specific iPSC-CMs (Figure 6B). Importantly,

Figure 5 Continued. (*tropomyosin 1*)-*L185F* mutation-introduced iPSC-CMs (Mut-int1, MUT-int1/MUT-int). **B**, Representative ×63 confocal images of patient and TPM1-L185F Mut-int1 iPSC-CMs treated with CV and Rho activator II (3 µg/mL, 3 hours) followed by immunostaining with a PIP2 antibody. Scale bar, 20 µm. Enlarged regions were zoomed in 5×. **C** and **D**, Quantification of **B**. ***$P<0.001$ for CV vs RhoA II Patient ($P=6.36\times10^{-3}$) and CV vs Rho A II Mut-int 1 ($P=6.68\times10^{-5}$) iPSC-CMs (Mann-Whitney *U* test). **E** and **F**, Rho activator II treatment assists the uptake of transferrin in Mut-int1 iPSC-CMs. **E**, Representative confocal images of Mut-int1 iPSC-CMs after control vehicle (CV) and RhoA II (3 µg/mL, 3 hours) treatment followed by incubation with Alexa 488–labeled transferrin (20 µg/mL, 5 minutes). Scale bar, 20 µm. Enlarged regions were zoomed in 5×. **F**, Quantification of **E**. Data are normalized by value from 0 minute. **$P<0.01$ ($P=2.30\times10^{-3}$) for CV vs RhoA II in Mut-int1 iPSC-CMs (Mann-Whitney *U* test). **G** and **H**, Abnormal early endosome distribution is rescued by RhoA II treatment in Mut-int1 iPSC-CMs. Confocal images (**G**) and quantification (**H**) of immunostaining with an anti-EEA1 antibody following CV and RhoA II (3 µg/mL, 3 hours) treatment. Scale bar, 20 µm. Enlarged regions were zoomed in 5×. ***$P<0.001$ for CV vs RhoA II ($P=2.51\times10^{-5}$; Mann-Whitney *U* test). **I** and **L**, Mitochondrial Fe (II) levels in DCM patient–derived WT (wild type)/MUT (mutation; Pat) and *TPM1-L185F MUT-int/MUT-int* iPSC-CMs were replenished following RhoA II treatment. **I** and **K**, CV or RhoA II (3 µg/mL, 3 hours) treatment followed by Mitotracker and FerroOrange staining. Representative ×63 confocal images are shown. Scale bar, 20 µm. Enlarged regions were zoomed in 5×. **J** and **L**, Region of interest (ROI)–based quantification of **I** and **K**. ***$P<0.001$ for control vehicle (CV) vs RhoA II in DCM patient–derived iPSC-CMs (Pat; $P=1.19\times10^{-5}$) and CV vs RhoA II in Mut-int1 ($P=6.34\times10^{-4}$) iPSC-CMs (Mann-Whitney *U* test). **M** through **P**, RhoA activation (1 µg/mL, 16 hours) improved mitochondrial respiration in both DCM patient–derived (**M** and **N**) and Mut-int1 (**O** and **P**) iPSC-CMs. **M** and **O**, Basal oxygen consumption rate (OCR) was improved by RhoA II treatment. **N** and **P**, A complete diagram of mitochondrial respiration recorded via a Seahorse XF analyzer is shown. **$P<0.01$ for patient CV vs patient RhoA II ($P=2.44\times10^{-4}$; Mann-Whitney *U* test). ***$P<0.001$ for Mut-int1 CV vs Mut-int1 RhoA II ($P<1\times10^{-15}$; Mann-Whitney *U* test). **Q**, Contractility in *TPM1-L185F MUT-int/MUT-int* iPSC-CMs. Delta F/F0 was recovered after RhoA II treatment (3 µg/mL, 3 hours). ***$P<0.001$ for CV vs RhoA II in Mut-int1 ($P=5.07\times10^{-7}$) iPSC-CMs (Mann-Whitney *U* test). **R** through **T**, RhoA II treatment resulted in increased sarcomere length in DCM patient–derived WT/MUT (Pat) iPSC-CMs and MUT-int/MUT-int TPM1-L185F iPSC-CMs, compared to respective control vehicle (CV). **R**, Representative ×63 confocal images of DCM patient–derived WT/MUT (Pat) and *TPM1-L185F MUT-int/MUT-int* iPSC-CMs treated with CV and RhoA II (3 µg/mL, 16 hours) followed by coimmunostaining with TnT (troponin T) and SAA (sarcomeric alpha-actinin) antibodies. Scale bar, 20 µm. Enlarged regions were zoomed in 5×. **S** and **T**, Quantification of **R**. *$P<0.05$ for CV vs RhoA II in patient ($P=0.0363$) and CV vs RhoA II in Mut-int1 ($P=0.0231$) iPSC-CMs as calculated by Mann-Whitney *U* test. Data are shown as mean ± sem. Images shown in figures are representative of the average value of each group. Unless indicated otherwise, the number of independent experiments equals the number of independent iPSC cardiac differentiations. Data points per experiment are shown as different shapes: # 1 as circles, #2 as triangles, #3 as squares, #4 as diamonds, #5 as crosses, #6 as stars. Au indicates arbitrary units.

compared to DCM patient–specific iPSC-CMs, uptake of the transferrin receptor (Figure 6C and 6D) as well as distribution of endosomes was rescued in isogenic Mut-cor iPSC-CMs (Figure 6E and 6F). Consequently, we noted mitochondrial iron levels to be >2-fold increased (DCM patient: 0.21±0.01 versus Mut-cor:0.52±0.03) following correction of the DCM mutation (Figure 6G and 6H). Consistently, Mut-cor iPSC-CMs displayed an increased mitochondrial respiration compared to DCM patient–derived iPSC-CMs (Figure 6I and 6J). Importantly, Mut-cor iPSC-CMs displayed improved sarcomere protein organization (Figure 6K and 6L) as well as recovered beating force (Figure 6M), compared to DCM patient–specific iPSC-CMs. As a control, we tested if small molecule-based treatment with UNC3230 or Lat-A could reintroduce disease phenotypes into DCM patient–derived, CRISPR/Cas9 Mutation-corrected iPSC-CMs. We measured basal mitochondrial respiration of Mut-cor iPSC-CMs in presence of UNC3230 or Lat-A, and found the oxygen consumption rate reduced, compared with control vehicle (Figure S11Q through S11T), which corroborated our findings.

To further investigate RhoA II-dependent rescue of pathophenotypes caused by dysfunction of the CME-dependent signaling pathway in presence of DCM mutations, we applied intracellular iron restriction by deferoxamine, a strong Fe(III) chelator.[80–82] As expected, deferoxamine treatment resulted in reduced mitochondrial iron levels in Mut-cor iPSC-CMs compared to control vehicle (Figure 6N and 6O). Of note, RhoA activation by RhoA II cotreated with deferoxamine reversed this effect (Figure 6N and 6O). Moreover, deferoxamine treatment decreased the contractility of Mut-cor iPSC-CMs, which we considered to present a consequence of decreased mitochondrial iron levels (Figure 6P), due to dysfunction of the CME-dependent signaling pathway. Importantly, RhoA activation by RhoA II delivered in parallel with deferoxamine treatment reversed this effect, resulting in improved contractility (Figure 6P). This further supported that RhoA activation delivered efficient rescue of molecular pathophenotypes such as reduced mitochondrial iron levels due to defective CME-dependent signaling in DCM iPSC-CMs. To further demonstrate the beneficial effects of RhoA activation on the CME signaling pathway, we treated Mut-cor iPSC-CMs with TFR (transferrin receptor) antibody to block the TFR[74] which efficiently blocked transferrin uptake in Mut-cor iPSC-CMs (Figure S12A and S12B). As expected, TFR antibody treatment resulted also in decreased mitochondrial iron levels, as a consequence of reduced CME-mediated iron uptake in the presence of TFR antibody (Figure 6Q and 6R). Cotreatment of RhoA II together with TFR antibody reversed the reduction of mitochondrial iron levels delivered by TFR antibody treatment (Figure 6Q and 6R). Moreover, TFR antibody treatment resulted in reduced contractility (Figure 6S) due to limited mitochondrial iron levels. As expected, RhoA activation ameliorated this effect when cotreated together with TFR antibody (Figure 6S), resulting in increased mitochondrial iron levels in the presence of TFR antibody. In line with this, TFR antibody treatment reduced the mitochondrial oxygen consumption rate of WT1 and Mut-cor iPSC-CMs (Figure S12C through S12F) due to impaired uptake of transferrin-bound iron and diminished mitochondrial iron levels in presence of the TFR antibody. Of note, RhoA II–mediated RhoA activation was able to achieve a robust rescue in presence of moderate concentrations of TFR antibodies which do not block all transferrin receptor molecules at the PM (Figure 6Q through 6S). Thus, RhoA II-dependent activation can boost CME-dependent signaling via the remaining unblocked TFR sites, while these are blocked in presence of higher concentrations of TFR antibody, diminishing the RhoA II–mediated recovery (Figure S12G).

Heart Tissues From Patients With DCM With End-Stage HF Display Defective Endosome Distribution

We considered that the mitochondrial iron deficiency due to defective endocytosis and endosome distribution observed in DCM iPSC-CMs may be present more generally in patients with HF. To test this, we analyzed vinculin-positive PM regions, where CME can initiate and endosomes can form, in the cardiomyocytes of left ventricular (LV) tissues from patients with end-stage HF due to DCM versus patients with preserved systolic LV function in the control group (Figure 7A through 7C; Tables S2 and S3 provide detailed clinical patient information). We found the vinculin-positive PM domains in patients with DCM with end-stage HF to be more disorganized and less regular than in the controls (Figure 7C). Moreover, we quantified the endosome distribution in cardiomyocytes of LV tissues from patients with DCM with end-stage HF versus patients with preserved systolic LV function in the control group. We utilized as an endosome marker CCDC53 (coiled-coil domain-containing protein 53), a subunit of the WASH (Wiskott-Aldrich syndrome protein and scar homolog) complex localized on endosomes.[83] In heart tissues from both patient groups, standard expression of TnT and CCDC53 was observed (Figure S13A and S13B). Strikingly, cardiomyocytes in LV tissues from patients with HF were characterized by higher levels of PM-localized endosomes, compared to controls with preserved LV function (Figure 7D through 7F; Figure S14A through S14E). Hence, these data closely recapitulate in the heart tissue of patients with HF both the disrupted PM-localized microdomains that present the basis for endosome formation, as well as the ectopic PM-localized endosome distribution. Thus, our findings suggest that the molecular dysfunctions caused by defective endocytosis and iron deficiency in

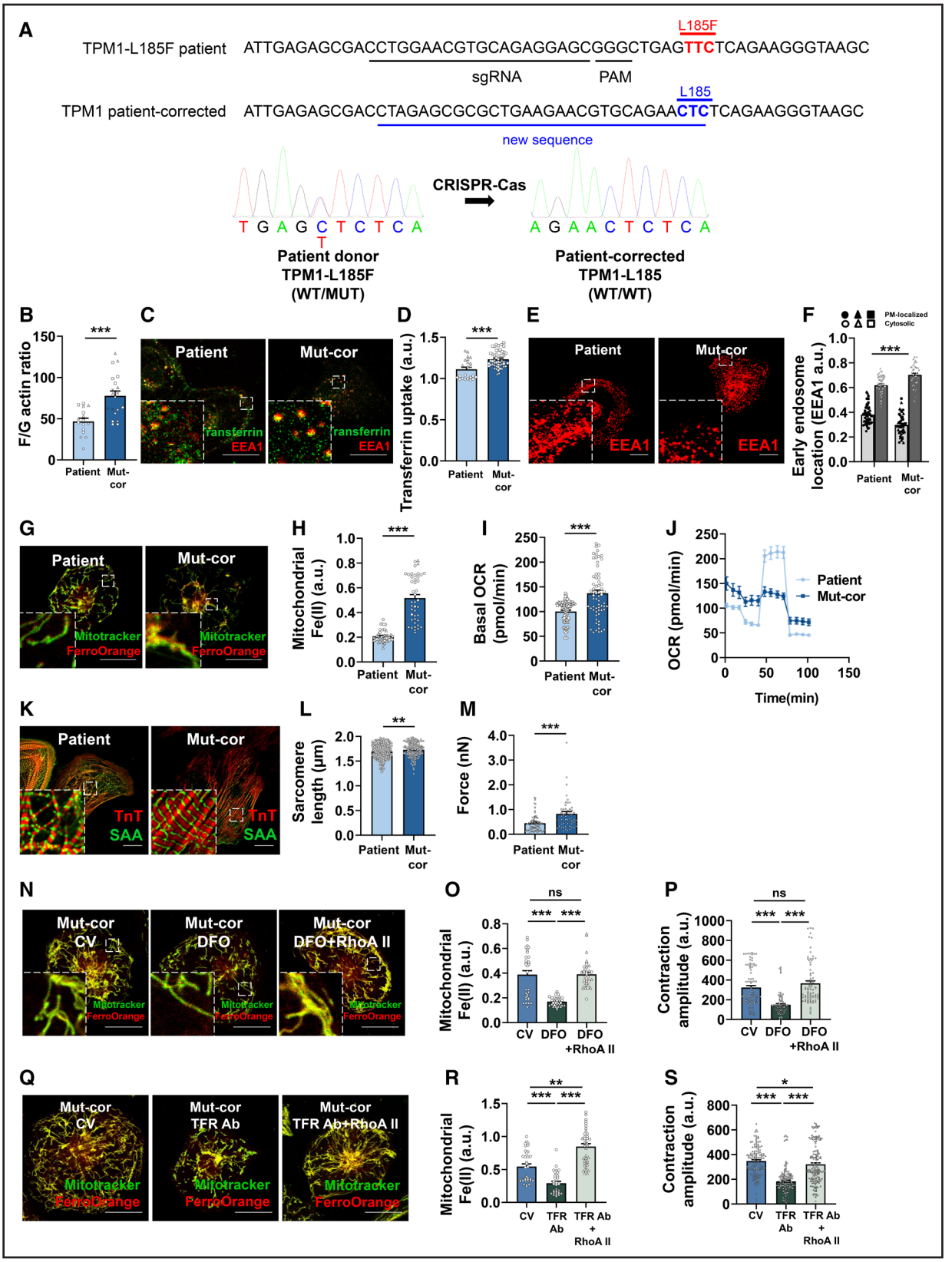

Figure 6. CRISPR/Cas9-correction of the patient-specific dilated cardiomyopathy (DCM) mutation *TPM1 (tropomyosin 1)-L185F* rescues endosome distribution and mitochondrial iron levels in DCM-corrected induced pluripotent stem cell–derived cardiomyocytes (iPSC-CMs).

A, CRISPR/Cas9 gene editing strategy to generate TPM1-L185F mutation-corrected iPSCs (WT [wild type]-cor/WT-cor) iPSCs. **B**, Increased fibrous actin (F-actin) content in WT-cor/WT-cor iPSC-CMs compared to DCM TPM1-L185F patient–derived WT/MUT (Pat) iPSC-CMs. Actin polymerization was measured via phalloidin (to stain F-actin) and DNase I (to stain G-actin) labeling in a high-content plate reader. (*Continued*)

the presence of DCM mutations may present a more general feature in patients with HF.

We also tested whether the expression levels of key proteins in the CME pathway in adult human heart tissues (healthy controls and patients with DCM) were corresponding to our observations made with DIA-MS in iPSC-CMs (Figure 1) as well as immunoblot assessment of iPSC-CMs (Figure S3L through S3O). Clinical data of healthy controls and patients with DCM are presented in Tables S2 and S3 as well as the Materials and Methods section. We found that protein expression levels of WASL (WASP like actin nucleation promoting factor) were upregulated in heart tissues of patients with DCM compared to healthy controls (Figure S14F through S14H), consistent with results from the DIA-MS experiments (Figure 1). A strong intraindividual and experimental variation was observed in analysis of the human heart tissues from different patients.

We next tested whether activity of the CME-dependent signaling pathway could be detected also in live adult patient–derived cardiomyocytes. Therefore, we established the measurement of CME-dependent uptake of transferrin-bound iron in live myocytes isolated from the right atrium of patients receiving open-heart coronary bypass cardiac surgery. Clinical data for these patients are presented in Table S4. Our results confirmed successful measurement of CME-dependent transferrin uptake in live adult cardiomyocytes (Figure 8A and 8B). Subsequently, we sought to test if CME-dependent signaling could be activated in live adult patient cardiomyocytes as well. We performed transferrin uptake assays in live adult cardiomyocytes from patients that were previously treated with RhoA II or control vehicle (Figure 8A and 8B). Our findings demonstrated increased transferrin uptake in the presence of RhoA II-dependent activation of RhoA in live adult cardiomyocytes, compared to control vehicle (Figure 8A and 8B). These experiments revealed that strikingly, Rho A activation presents a viable option to modulate CME-dependent signaling in live

Figure 6 Continued. Normalization to cell numbers labeled by DAPI is performed. ***P<0.001 (P=9.011×10^{-4}) for DCM patient–derived (Pat) vs mutation-corrected (Mut-cor) iPSC-CMs (Mann-Whitney U test). Data of mutation-corrected (Mut-cor) iPSC-CMs were compared to data from DCM patient–derived (Pat) group in Figure 3A. **C** and **D**, Increased transferrin uptake in WT-cor/WT-cor iPSC-CMs. **C**, Representative images of DCM patient–derived (Pat, WT/MUT) and patient-derived, Cas9-mutation–corrected (WT-cor/WT-cor) iPSC-CMs after incubation with Alexa 488–labeled transferrin (20 µg/mL, 5 minutes). Scale bar, 20 µm. Enlarged regions were zoomed in 5×. **D**, Quantification of **C**. Data are normalized by uptake at 0 minute; scale bar, 20 µm. ***P<0.001 (P=1.63×10^{-4}) for DCM patient–derived (Pat) vs mutation-corrected mut-cor iPSC-CMs (Mann-Whitney U test). Data of mutation-corrected (Mut-cor) iPSC-CMs were compared with data from DCM patient–derived (Pat) group in Figure 3E. **E** through **F**, Abnormal early endosome distribution is rescued mutation-corrected iPSC-CMs. Confocal images (**E**) and quantification (**F**) of cells immuno-stained with an anti-EEA1 antibody. Scale bar, 20 µm. Enlarged regions were zoomed in 5×. ***P<0.001 for DCM patient–derived (Pat) vs mutation-corrected (Mut-cor) iPSC-CMs (P=1.308×10^{-5}; Mann-Whitney U test). Data of mutation-corrected (Mut-cor) iPSC-CMs were compared to data from DCM patient–derived (Pat) group in Figure 3G. **G** and **H**, Increased mitochondrial Fe (II) levels in mutation-corrected iPSC-CMs. **G**, Representative ×63 confocal images following Mitotracker and FerroOrange staining. Scale bar, 20 µm. Enlarged regions were zoomed in 5×. **H**, Region of interest (ROI)–based quantification of **G**. ***P<0.001 for DCM patient–derived (Pat) vs mutation-corrected (Mut-cor) iPSC-CMs (P<1×10^{-15}; Mann-Whitney U test). **I** and **J**, Basal oxygen consumption rate (OCR) was rescued by genomic correction. **I**, Mut-cor iPSC-CMs display increased basal OCR compared to DCM patient–derived iPSC-CMs. **J**, A complete diagram of mitochondrial respiration recorded via a Seahorse XF analyzer is shown. ***P<0.001 for patient vs mut-cor iPSC-CMs (P=3.54×10^{-6}; Mann-Whitney U test). Data of mutation-corrected (Mut-cor) iPSC-CMs were compared to data from DCM patient–derived (Pat) group in Figure 4C and 4D. **K** and **L**, Increased sarcomere length observed in mutation-corrected iPSC-CMs (WT-cor/WT-cor) compared to DCM patient–derived (WT/MUT) iPSC-CMs. **K**, Representative ×63 confocal images of DCM patient–derived (WT/MUT) and mutation-corrected iPSC-CMs following immunostaining with anti- TnT (troponin T) and anti-SAA (sarcomeric alpha-actinin) antibodies. Scale bar, 20 µm. Enlarged regions were zoomed in 5×. **L**, Quantification of **K**. **P<0.01 for DCM patient–derived (Pat) vs mutation-corrected (Mut-cor) iPSC-CMs (P=6.62×10^{-3}; Mann-Whitney U test). Data of mutation-corrected (Mut-cor) iPSC-CMs were compared to data from DCM patient–derived (Pat) group in Figure 2C. **M**, Increased contractile force in mutation-corrected (WT-cor/WT-cor) compared to DCM patient–derived (WT/MUT) iPSC-CMs. ***P<0.001 for DCM patient–derived (Pat) vs mutation-corrected (Mut-cor) iPSC-CMs (P=5.36×10^{-5}; Mann-Whitney U test). Data of mutation-corrected (Mut-cor) iPSC-CMs were compared to data from DCM patient–derived (Pat) group in Figure 2D. **N** and **O**, Deferoxamine (DFO) treatment in Mut-cor iPSC-CMs results in reduced mitochondrial iron levels. RhoA II (Rho activator II) treatment in presence of DFO rescues mitochondrial iron levels in Mut-cor iPSC-CMs. **P**, Representative ×63 confocal images of live cells stained with Mitotracker Green and FerroOrange. Scale bar, 20 µm. Enlarged regions were zoomed in 5×. **O**, Quantification of **N**. ***P<0.001 for control vehicle (CV) vs DFO (P=1.47×10^{-8}) and DFO vs DFO+RhoA II (P=8.41×10^{-11}). ns, not significant for CV vs DFO +RhoA II (Kruskal-Wallis test and Dunn multiple comparisons test). **P**, DFO treatment reduces the contraction amplitude in Mut-cor iPSC-CMs. Cotreatment of RhoA II in presence of DFO recovers the reduced contraction amplitude mediated by DFO in Mut-cor iPSC-CMs. ***P<0.001 for CV vs DFO (adjusted P=3.47×10^{-12}) and DFO vs DFO+RhoA II (adjusted P<1×10^{-15}). ns, not significant for CV vs DFO+RhoA II (Kruskal-Wallis test and Dunn multiple comparisons test). **Q** and **R**, TFR antibody (Ab) treatment reduces mitochondrial iron levels in Mut-cor iPSC-CMs. RhoA II treatment in presence of TFR Ab recovers mitochondrial iron levels in Mut-cor iPSC-CMs. **Q**, Representative ×63 confocal images of live cells stained with Mitotracker Green and FerroOrange. Scale bar, 20 µm. Enlarged regions were zoomed in 5×. **R**, Quantification of **Q**. ***P<0.001 for CV vs TFR Ab (adjusted P=1.19×10^{-4}) and TFR Ab vs TFR Ab+RhoA II (adjusted P=9×10^{-15}); **P<0.01 for CV vs TFR Ab+RhoA II (adjusted P=7.05×10^{-4}; Kruskal-Wallis test and Dunn multiple comparisons test). **S**, TFR Ab treatment results in a reduced contraction amplitude in Mut-cor iPSC-CMs. RhoA II treatment in parallel with TFR Ab recovers the contraction amplitude in Mut-cor iPSC-CMs. ***P<0.001 for CV vs TFR Ab (adjusted P<1×10^{-15}) and TFR Ab vs TFR Ab+RhoA II (P<1×10^{-15}); *P<0.05 for CV vs TFR Ab +RhoA II (adjusted P=0.047; Kruskal-Wallis test and Dunn multiple comparisons test). Data are shown as mean±SEM. Images shown in figures are representative of the average value of each group. Unless indicated otherwise, the number of independent experiments equals the number of independent iPSC cardiac differentiations. Data points per experiment are shown as different shapes: #1 as circles, #2 as triangles, #3 as squares, #4 as diamonds, #5 as crosses, #6 as stars. Au indicates arbitrary units; and F/G actin, fibrous/globular actin.

myocytes from adult patients. Overall, our findings suggest a new pathomechanism in patients with DCM due to inherited mutations as well as in patients with DCM with systolic HF. Sarcomere protein misalignment may destabilize protein-protein interactions linking sarcomeres and other cytoskeleton filaments to the PM and contribute to defective functions of PIP2-enriched PM microdomains critical for CME. Consequently, endosome formation and distribution are impaired, resulting in reduced uptake of critical cargo such as transferrin-bound iron and lower mitochondrial iron levels (Figure 8C). These molecular defects can contribute to reduced energy supply and impaired contractility of cardiomyocytes in patients with DCM and HF. Of note, we showed that activity of the newly described CME-dependent signaling pathway can be detected and modulated also in live adult cardiomyocytes from patients.

DISCUSSION

Iron deficiency is a comorbidity in 50% of patients with HF[1] and may present a therapeutic target.[6] Main causes for iron deficiency at the organ level are intestinal iron absorption and circulation-related defects as well as impaired iron retention in HF. In addition, despite insights into molecular disease mechanisms at the cellular level, DCM remains a main cause of HF and new therapeutic directions are needed. Mutations in genes encoding sarcomere proteins have been identified to cause 30% of DCM cases.[20,84] Genetic models of DCM[85–87] have been employed to elucidate the molecular causes of primary dysfunctions observed in the presence of DCM mutations, such as disrupted sarcomere protein organization and defective contractility.[23,87–89] Recently, impaired protein-based interactions of the sarcomeres with other cytoskeleton filaments have been shown to contribute to DCM disease phenotypes in patient-specific iPSC-CMs.[23,55] However, the subcellular dysfunctions in presence of DCM mutations at the molecular and signaling levels are to date still incompletely understood. Based on this, we generated here a human iPSC-CM model of the new DCM-causing mutation *TPM1-L185F*, combined with CRISPR/Cas9-based gene editing to elucidate molecular dysfunctions in the presence of DCM mutations, such as consequences of defective sarcomere organization and functions. We identified sarcomere interactions via the stabilizing PM-binding protein vinculin to be disrupted in the presence of 2 different DCM mutations, *TPM1-L185F* and *TnT-R141W*. Consequently, this disrupted vinculin-containing and F-actin–organizing PM hubs enriched for PIP2 in DCM iPSC-CMs. Altered F-actin–binding PIP2 microdomains at the PM, in turn, resulted in defective CME of critical cargo such as transferrin-bound iron in DCM iPSC-CMs. These findings establish defective endocytosis and impaired distribution of endosome cargo carries as a molecular basis for mitochondrial iron deficiency in the presence of DCM mutations. Importantly, we could rescue this pathogenic mechanism in a 3-fold way in our human iPSC-CM model: First, by treatment with Rho activator II[77] which replenished PM PIP2 levels and rescued CME, endosome distribution, as well as mitochondrial iron levels and DCM iPSC-CM contractility. Second, supplying iron externally could overcome depletion of mitochondrial iron deficiency and rescue contractility in DCM iPSC-CMs. Third, these phenotypic dysfunctions were recovered in iPSC-CMs following CRISPR/Cas9–based correction of the inherited DCM mutation, *TPM1-L185F*, in patient-specific iPSCs. Moreover, we phenocopied the pathomechanistic defects found in presence of the *TPM1-L185F* mutation into WT control iPSC-CMs via drug treatments targeting the disease pathway: Application of a small molecule inhibitor of actin polymerization (Lat-A) introduced defective endosome distribution in WT control iPSC-CMs. Furthermore, treatment with a PIP5K inhibitor (UNC3230) introduced in WT control iPSC-CMs disruption of F-actin/PIP2-containing PM microdomains, the sites of CME and endosome formation.

Interestingly, cardiac-specific overexpression of RhoA ultimately induces DCM with impaired contractility[90] and treatment with an inhibitor of the well-characterized downstream effector of RhoA, ROCK (Rho-associated protein kinase), protected the heart against ischemia/reperfusion injury.[91] Treatment with an inhibitor of ROCK benefited patients with cardiac hypertrophy in clinical trials.[92,93] However, the complete deletion of RhoA from cardiomyocytes results in accelerated DCM and increases the severity of HF outcome following chronic pressure overload.[78] These reports indicate the critical need for fine-tuned modulation of RhoA activity as a basis for cardiomyocyte homeostasis and recovery in disease models. In line with this, low levels of constitutively active RhoA in cardiomyocytes protected mouse hearts against ischemia/reperfusion injury and improved contractile function.[94] Consistently, our findings showed that low-dose activation of RhoA improved sarcomere-PM interactions via vinculin and F-actin. Concomitantly, RhoA treatment replenished PIP2 content at the PM and recovered CME and endosome distribution in DCM iPSC-CMs.

The signaling mechanisms associated with systemic iron deficiency in HF due to absorption defects are complex.[2,6,7,95] It should be noted that both the inappropriate elevation and reduction of iron levels are associated with cardiac disease,[34,35] indicating the importance of intact iron homeostasis. Abnormally high iron levels lead to iron overload cardiomyopathy[35] while abnormally low levels of iron were linked to cardiovascular disease as well.[3–5] Iron homeostasis at the systemic level, including the storage and export of excess iron, is mediated by ferritin, ferroportin, and iron regulatory proteins IRP1 (iron responsive protein 1; ACO1 [aconitase 1]) and IRP2 (IREB2 [iron responsive element binding protein 2]).[3,96–98] Low iron

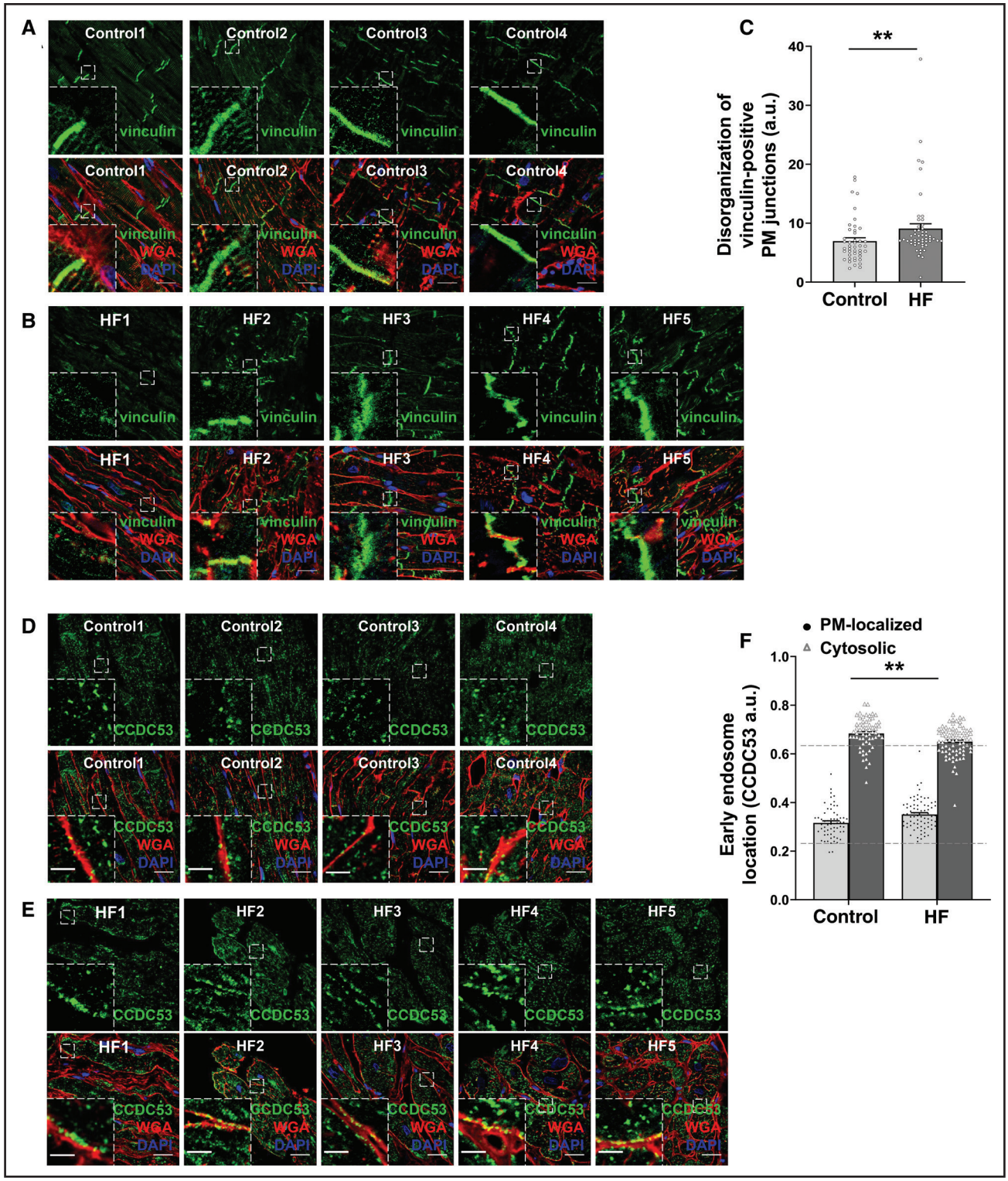

Figure 7. Heart tissues from patients with dilated cardiomyopathy (DCM) with end-stage heart failure (HF) display defective endosome distribution.

Assessment of vinculin-positive plasma membrane (PM) regions where clathrin-mediated endocytosis (CME) may initiate and endosomes may form, as well as analysis of the intracellular distribution of endosomes were performed by immunostaining in human heart tissue. Left ventricular (LV) heart tissue from patients with dilated cardiomyopathy who received a heart transplantation due to severe HF (indicated as HF, or heart transplantation) was analyzed. In comparison, LV heart tissue from patients with preserved LV function that underwent aortic valve replacement (severe valve stenosis) and coronary artery bypass graft surgery was used in the control group ("control"). **A** through **C**, LV tissues from patients with DCM with HF show disorganized PM-localized vinculin-positive regions compared to controls. Representative ×63 confocal images of tissues from control (**A**) vs HF (**B**) stained with WGA (wheat germ agglutinin, Alexa Fluor 594 Conjugate) and a vinculin antibody. (*Continued*)

levels have been shown to induce IRP1/2-modulated increase of iron uptake via stabilization of TfR1-encoding mRNAs, while IRP-dependent repression of ferritin and ferroportin mRNA translation reduces iron sequestration as well as export.[99] Mitochondria utilize a major amount of intracellular iron in Fe/S clusters as well as heme groups essential for the function of electron transport chain complexes.[71] Insufficient iron levels impair mitochondrial function in cardiomyocytes[3,100] which may occur by enhanced degradation of mRNAs encoding mitochondrial Fe/S-cluster-containing proteins.[72,100] In line with this, we found iron supplementation to rescue both mitochondrial iron levels as well as iPSC-CM contractility in DCM iPSC-CMs. Importantly, clinical trials demonstrated intravenous iron administration to improve end point outcomes in HF patients, including improvement of New York Heart Association class, increased 6-minute walking distance, and improved quality of life.[8–10,101] These results were independent of the presence of anemia. Here, our data demonstrated that iron deficiency occurs in DCM iPSC-CMs as a consequence of DCM mutations in sarcomere proteins, which lead to impaired protein-protein interactions between the sarcomeric cytoskeleton and the PM. These further result in defective actin polymerization at the PM, a critical step for CME-dependent cargo uptake. Consequently, impaired CME-dependent iron uptake leads to reduced mitochondrial iron levels. Mitochondria are major consumers of intracellular iron, which they require to produce Fe/S clusters and heme groups that are essential for the function of complexes I to IV in the electron transport chain and contribute to oxidative phosphorylation.[71] Reduced mitochondrial iron levels impair mitochondrial respiration and energy production.[72] Because cardiomyocytes require high amounts of energy to maintain their essential functions, such as contractile force generation, impaired mitochondrial function resulting in reduced energy supply is detrimental for cardiomyocytes and results in reduced contractility.[72] Here, we confirmed that sarcomeric DCM mutations trigger a pathomechanism that causes defective CME-dependent cargo uptake, thereby resulting in decreased mitochondrial iron levels and contributing to impaired contractility in DCM (MUT) iPSC-CMs. It should be noted that DCM iPSC-CMs display defective contractility primarily due to the substantial disruption of sarcomeres due to the DCM mutations. However, the defective contractility is exacerbated in DCM iPSC-CMs by defective CME-dependent signaling which limits mitochondrial iron levels and mitochondrial respiration. Consistently, iron supplementation can only deliver a partial rescue of the impaired contractility in DCM iPSC-CMs, which further highlights the importance of balanced iron levels to maintain cardiomyocyte contractility. We confirmed that CRISPR/Cas9–based genomic correction of the DCM mutation *TPM1-L185F* rescued mitochondrial iron levels and contractile force generation. In addition, we found that RhoA activation via RhoA II presents another means of rescuing molecular pathophenotypes in presence of DCM mutations, such as depleted mitochondria iron levels and impaired contractility. RhoA II increase the PIP2 production and actin polymerization at the PM and thereby recovers transferrin uptake, mitochondrial iron levels, and contractility in DCM iPSC-CMs. This is in line with a previous study showing that defective RhoA activation leads to severely impaired transferrin uptake.[102]

Moreover, our experiments using a DMT1 inhibitor, ebselen,[74] confirmed that uptake of the major amount of intracellular iron via CME-based internalization of transferrin-bound ferric iron, Fe(III), occurs independently of DMT1. Likewise, uptake of LDL, another critical intracellular cargo internalized into cardiomyocytes via CME, is not dependent on supplementation with ferro iron, Fe(II). The DMT1 porter, on the other hand, is known to regulate intracellular uptake of ferro iron, Fe(II), under the control of the IRP/IRE (iron-responsive element) post-translational regulation system.[103] The DMT1-dependent uptake of ferro iron, Fe(II), is also independent of other cellular uptake processes such as phagocytosis, as supplementation with ferro iron, Fe(II), does not alter phagocytosis. In summary, we report that sarcomeric DCM mutations lead to impaired PIP2 production and reduced actin polymerization at the PM, causing defective CME-dependent signaling and thereby resulting in depleted mitochondrial iron levels as well as respiration, which enhances defective contractility in DCM iPSC-CMs. These new findings are in line with previous reports of animal models with a titin-truncating DCM variant displaying mitochondrial dysfunction such as decreased oxygen consumption rate, and increased levels of reactive oxygen species in cardiomyocytes.[104] Mitochondrial defects were also recorded in a murine model of a DCM-causing LMNA mutation.[105]

Figure 7 Continued. Scale bar, 20 µm. Enlarged regions were zoomed in 5×. **C**, Quantification of **A** and **B** using ImageJ. Data display the SE of mean of angles from vinculin-positive areas in each image. Control, n=45 images, n=4 patients; HF, n=52 images, n=5 patients; corresponding data points were used for analysis. $^{**}P<0.01$ for control vs HF ($P=0.00187$; Mann-Whitney *U* test). **D** through **F**, LV tissues from patients with DCM with HF show abnormal early endosome (EE) distribution with the EEs localizing to the PM compared to controls. Representative ×63 confocal images of tissues from control (**D**) vs HF (**E**) stained with WGA (Alexa Fluor 594 Conjugate) and a CCDC53 (coiled-coil domain-containing protein 53) antibody. Scale bar, 20 µm (scale bar in enlarged sections, 5 µm). Enlarged regions were zoomed in 5×. **F**, Quantification of immunostaining and confocal images as described in (**D** and **E**) using ROI-based image quantification via ImageJ. Control, n=61 images, n=4 patients; HF, n=76 images, n=5 patients; corresponding data points were used for analysis. $^{**}P<0.01$ for control vs HF ($P=0.00121$; Mann-Whitney *U* test). Data are shown as mean±SEM. Images shown in figures are representative of the average value from each group. Au indicates arbitrary units; and DAPI, 4′,6-diamidino-2-phenylindole.

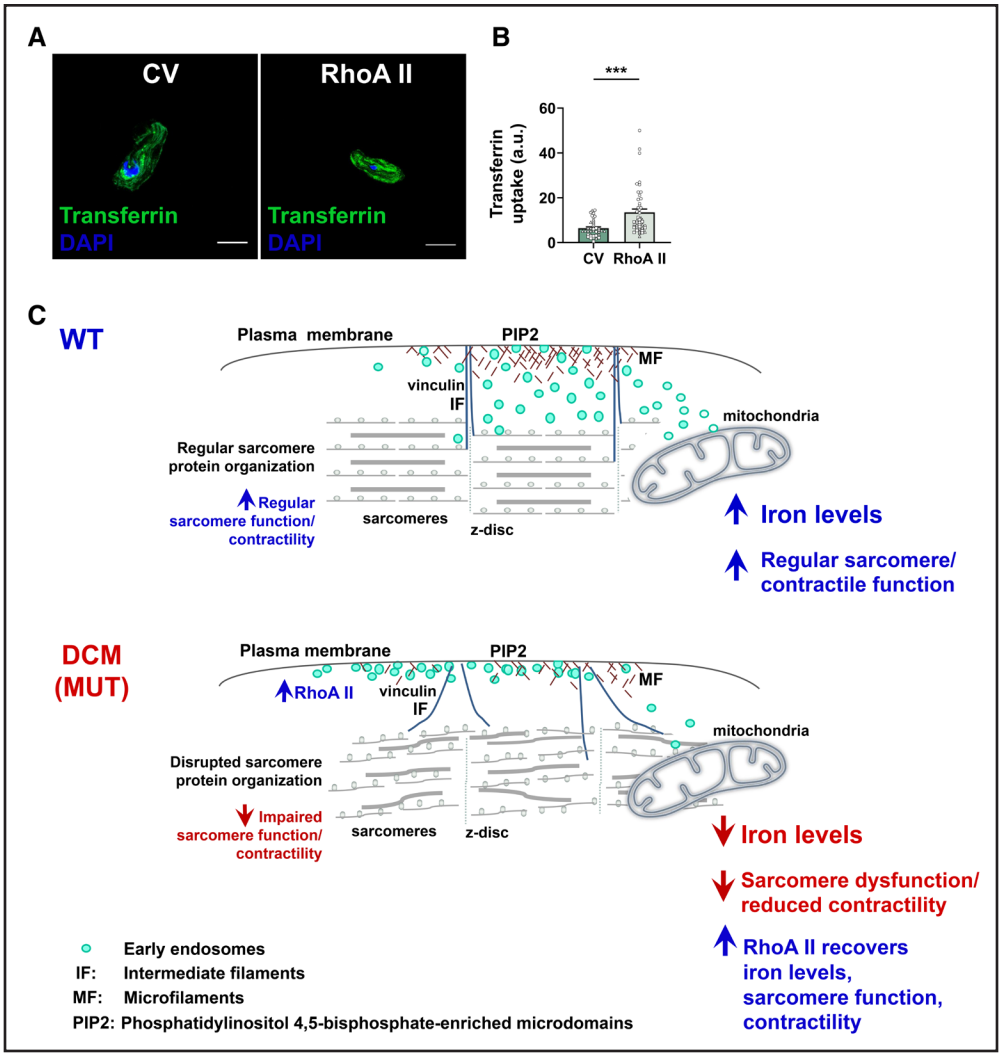

Figure 8. Defective endocytosis and endosome distribution result in mitochondrial iron deficiency in the presence of dilated cardiomyopathy (DCM) mutations.

Activity of the clathrin-mediated endocytosis (CME)–dependent signaling pathway was detected in live atrial cardiomyocytes obtained from tissue of patients undergoing open-heart coronary bypass cardiac surgery by measuring transferrin uptake. RhoA II (Rho activator II) treatment activating RhoA increased CME-dependent transferrin uptake in live adult patient myocytes, compared to control vehicle. **A**, Representative ×63 confocal images are shown. Scale bar, 20 µm. **B**, Quantification of **A**. ***$P<0.001$ for control vehicle (CV) vs RhoA II ($P=1.21\times10^{-5}$; Mann-Whitney *U* test). **C**, Schematic indicating pathomechanisms associated with dysfunctional sarcomere links via vinculin to fibrous actin (F-actin)/phosphatidylinositol 4,5-bisphosphate (PIP2)–enriched plasma membrane (PM) microdomains, resulting in impaired clathrin-mediated endocytosis (CME) of cargo such as transferrin-bound iron, as well as altered endosome distribution. These molecular dysfunctions cause lower mitochondrial iron levels and reduced mitochondrial function, as well as impaired contractility and force generation. Disrupted sarcomere organization and function is observed in presence of DCM mutations as well as in cardiomyocytes from patients with systolic heart failure. Intermediate filaments (IF); actin filaments around the PM (MF; red); PIP2 denotes PIP2-enriched PM microdomains; green circles, endosomes containing transferrin-bound iron. Images shown in figures are representative of the average value of each group. Au indicates arbitrary units; and DAPI, 4′,6-diamidino-2-phenylindole.

Consistently, we found that DCM mutations in sarcomere proteins led to mitochondrial dysfunction, such as reduced oxygen consumption rate and increased levels of mitochondrial superoxide levels. Importantly, our study links the defective CME-dependent signaling pathway in DCM iPSC-CMs to mitochondrial dysfunction and defective contractility as end point phenotypes in DCM that are exacerbated by this pathomechanism. These findings were supported by chemical phenotype-introduce as well as phenotype-rescue experiments manipulating key points of the CME-dependent signaling pathway.

Here, we describe a new molecular iron uptake defect in cardiomyocytes unrelated to systemic iron absorption defects: the impaired subcellular uptake of transferrin-bound iron. This molecular pathomechanism is linked to the sarcomere disorganization observed not only in the presence of DCM mutations but also in the heart tissues of patients suffering from other forms of systolic HF. Our findings show that sarcomere disorganization results in disrupted vinculin-based linkage and formation of PM hubs enriched for F-actin and PIP2. These PM microdomain hubs are critical for initiation of endocytosis and

uptake of cargo such as transferrin-bound iron. Indeed, it could be expected that other pathophysiological dysfunctions may also interfere with endocytosis and cargo uptake, for example, by causing defective formation and/or function of F-actin and PIP2-enriched PM microdomains in other ways.

The majority of cardiomyocyte iron demand is served by TfR1-mediated internalization of the iron-carrier transferrin. We observed in DCM iPSC-CMs defective F-actin/PIP2-enriched microdomains at the PM, resulting in impaired endocytosis of transferrin-bound iron and, ultimately, reduced mitochondrial iron levels. This pathomechanism could be reversed by rescue of F-actin/PIP2 microdomain function via Rho activator II treatment, which consequently recovered uptake of transferrin and distribution of endosomes. This resulted in improved mitochondrial iron levels as well as contractility in DCM iPSC-CMs.

Moreover, this disease mechanism was confirmed by introducing defective F-actin/PIP2-dependent microdomain function via Lat-A treatment into WT iPSC-CMs. Concomitantly, Lat-A treatment induced impaired endosome distribution and decreased mitochondrial iron levels in the healthy donor-derived iPSC-CMs. While impaired contractility in presence of DCM mutations is primarily caused by sarcomere dysfunction, we showed this to be reversed following CRISPR/Cas9–based genomic correction of the DCM mutation in patient-derived iPSC-CMs. Interestingly, chemical and peptide treatments blocking function of the CME-dependent signaling pathway (Lat-A and UNC3230) reintroduced contractile dysfunction into the Mut-cor iPSC-CMs. These findings support that part of the impaired contractility observed in presence of DCM mutations could be due to downstream consequences resulting from defective sarcomere protein organization and function. We consider this an exciting perspective because secondary causes of contractile defects may be in some cases more amenable to therapeutic drug-based rescue, such as via RhoA II, than the primary sarcomere mutation itself.

Iron supplementation through DMT1-dependent Fe(II) uptake improved contractility in DCM iPSC-CMs which display defective CME-based uptake of transferrin-bound iron, Fe(III). This supported that DMT1 assisted cells to uptake nontransferrin-bound iron in its ferro form, Fe(II). Furthermore, this provided a line of evidence of treatments targeting DMT1 for patients with iron deficiency. Protein expression levels of the TFR were not significantly changed, suggesting that patients with DCM carrying inherited mutations might profit from iron supplementation also when transferrin levels in their blood are not abnormal. Yet, it should be noted that iron supplementation may not completely recover phenotypic consequences of HF in cases where the defects are located further downstream of the pathomechanism described here. Additionally, we found that Fe(II) treatment did not alter LDL uptake in presence of DCM mutations in sarcomere proteins. This indicated that Fe(II) treatment had no effect on CME-dependent cargo uptake. However, it is possible that enhanced availability of substrate such as ferric iron, Fe(III), could boost CME-based uptake of transferrin-bound ferric iron, Fe(III), as the CME pathway might not operate at maximum capacity under steady-state conditions. In vivo experiments in animal models, such as mice, would allow us to further address this point. Moreover, Fe(III) restriction via deferoxamine treatment led to reduced mitochondrial iron levels and impaired contractility. RhoA activation could rescue the disturbed mitochondrial iron levels and contractility in presence of deferoxamine. Furthermore, TFR antibody treatment in CRISPR/Cas9 Mut-cor (Mut-cor) iPSC-CMs, which display functions comparable to WT control, led to decreased mitochondrial iron levels and reduced contractility as a consequence of reduced CME-mediated iron uptake. Consistently, RhoA activation in Mut-cor iPSC-CMs in presence of TFR antibody reversed the reduced mitochondrial iron levels as well as impaired contractility. However, higher concentrations of TFR antibody increased the blockage of the transferrin receptor, which depressed the rescue effects delivered by a parallel RhoA II treatment. Together, these findings further supported our conclusions, supporting a balanced intracellular iron homeostasis in cardiomyocytes to be essential for proper cardiovascular functions. Currently, it is not known whether mechanisms may exist that link mutations in sarcomere proteins to regulation of iron homeostasis genes. Although the investigation of such mechanisms exceeds the frame of this study, this could be an interesting topic for future research. Subsequent studies could include animal models such as mouse models. Animal models are needed to investigate if ferric iron, Fe(III), supplementation could enhance CME-dependent iron uptake in vivo. Moreover, animal models would allow us to test if RhoA activation in presence of DCM mutations rescues defective CME-dependent signaling, impaired endosomal cargo distribution, and iron deficiency in vivo.

We showed that RhoA treatment improved contractility as well as sarcomere protein organization and interactions as well as PM microdomain function in DCM iPSC-CMs. These findings suggest a potential benefit of fine-tuned therapeutic modulation of RhoA activity for patients carrying inherited DCM mutations. Interestingly, we demonstrated that heart tissues from patients with DCM with end-stage HF display an abnormal distribution of endosome cargo carriers as well. These data suggest that iron deficiency due to defective endocytosis might present a more general dysfunction in patients with DCM with HF. Together, the pathomechanism of defective CME and endosome cargo distribution described here may possibly play a role in the pathophysiology of cardiomyopathy and HF and might be a prevalent mechanism in

presence of DCM mutations. Based on these findings, it will be relevant to explore if this disease mechanism may be true also for other forms of systolic HF. Of note, we established an assay for measuring CME-dependent cargo uptake of transferrin-bound iron also in live cardiomyocytes from adult patients. We demonstrated that the CME-dependent signaling pathway is active also in live cardiomyocytes from adult patients. Moreover, we showed that CME-dependent signaling can be activated by RhoA II treatment in live adult cardiomyocytes, suggesting that RhoA activation could constitute a potential druggable target in patients with DCM and HF. Overall, drug treatments addressing defects in this molecular mechanistic pathway may present promising future therapeutic directions for patients with DCM with inherited sarcomeric mutations.

ARTICLE INFORMATION

Received September 5, 2022; revision received May 23, 2023; accepted May 26, 2023.

Affiliations

Heart Research Center Goettingen, Clinic for Cardiology and Pneumology, University Medical Center Goettingen, Georg-August University of Goettingen, Germany (Y.D., N.I., H.X., R.W., K.T., S.B., S.S., E.M.Z., S.E.L., G.H., A.E.). DZHK (German Center for Cardiovascular Research), partner site Goettingen, Germany (Y.D., N.I., H.X., R.W., K.T., S.B., C.L., J.P., F.E.F., E.M.Z., I.K., N.V., S.E.L., G.H., A.E.). Heart Center, Clinic for Cardiology and Pneumology, University Medical Center Goettingen (K.T., S.B., S.S., G.H.), Department of Clinical Chemistry, University Medical Center Goettingen, (C.L., H.U.), Institute of Pharmacology and Toxicology, University Medical Center Goettingen, (J.P., F.E.F., N.V.), Institute for Physical Chemistry (A.J.), and Cluster of Excellence "Multiscale Bioimaging: from Molecular Machines to Networks of Excitable Cells" (MBExC; C.L., F.E.F., N.V., S.E.L.), University of Goettingen, Germany. Department for Internal Medicine II, University Medical Center Regensburg (S.S.). Department of Thoracic and Cardiovascular Surgery, University Medical Center Göttingen (I.K.). Bioanalytical Mass Spectrometry, Max Planck Institute for Multidisciplinary Sciences, Goettingen (C.L., H.U.). Department of Cardiology, Aarhus University Hospital, Denmark (T.B.R.). Department of Cardiology, Aalborg University Hospital, Denmark (J.M.).

Acknowledgments

This work was supported by the Deutsche Forschungsgemeinschaft (German Research Foundation) Collaborative Research Centers Sonderforschungsbereich (SFB) 1002, projects A09 (S. Brandenburg, C. Lenz, S.E. Lehnart), A12 (A. Ebert), A13 (N. Voigt), S02 (S.E. Lehnart) and SFB 1190 (H. Urlaub); and under Germany's Excellence Strategy - EXC 2067/1- 390729940; the Deutsche Stiftung für Herzforschung (DSHF) Projekt F/13/20 (A. Ebert), and the German Academic Exchange Service (Deutscher Akademischer Austauschdienst (DAAD; German Academic Exchange Service), N. Ignatyeva). N. Voigt (81X4300115, 81X4300112, 81X4300102) and A. Ebert (81X2300194, 81X4300123) are supported by Deutsches Zentrum für Herz-Kreislaufforschung e.V. (DZHK; German Center for Cardiovascular Research). G. Hasenfuss and S.E. Lehnart are principal investigators of DZHK (German Center for Cardiovascular Research). The authors are grateful for support by the DZHK (German Center for Cardiovascular Research), partner site Goettingen, Germany, and the Clinic for Cardiology and Pneumology at the University Medical Center, Goettingen University. The authors thank the Central Service Unit for Cell Sorting at the University Medical Center, Goettingen University for their support, and the Stem Cell Unit at the University Medical Center, Goettingen University.

Disclosures

None.

Supplemental Materials

Supplemental Methods
Figures S1–S14
Tables S1–S5
References 106–112

REFERENCES

1. Rizzo C, Carbonara R, Ruggieri R, Passantino A, Scrutinio D. Iron deficiency: a new target for patients with heart failure. *Front Cardiovasc Med.* 2021;8:709872. doi: 10.3389/fcvm.2021.709872
2. Ghafourian K, Shapiro JS, Goodman L, Ardehali H. Iron and heart failure: diagnosis, therapies, and future directions. *JACC Basic Transl Sci.* 2020;5:300–313. doi: 10.1016/j.jacbts.2019.08.009
3. Lakhal-Littleton S. Mechanisms of cardiac iron homeostasis and their importance to heart function. *Free Radic Biol Med.* 2019;133:234–237. doi: 10.1016/j.freeradbiomed.2018.08.010
4. Rocha BML, Cunha GJL, Menezes Falcao LF. The burden of iron deficiency in heart failure: therapeutic approach. *J Am Coll Cardiol.* 2018;71:782–793. doi: 10.1016/j.jacc.2017.12.027
5. von Haehling S, Jankowska EA, van Veldhuisen DJ, Ponikowski P, Anker SD. Iron deficiency and cardiovascular disease. *Nat Rev Cardiol.* 2015;12:659–669. doi: 10.1038/nrcardio.2015.109
6. Ponikowski P, Jankowska EA. Targeting iron deficiency in heart failure: existing evidence and future expectations. *Circ Heart Fail.* 2021;14:e008299. doi: 10.1161/CIRCHEARTFAILURE.121.008299
7. von Haehling S, Ebner N, Evertz R, Ponikowski P, Anker SD. Iron deficiency in heart failure: an overview. *JACC Heart Fail.* 2019;7:36–46. doi: 10.1016/j.jchf.2018.07.015
8. Anker SD, Comin Colet J, Filippatos G, Willenheimer R, Dickstein K, Drexler H, Lüscher TF, Bart B, Banasiak W, Niegowska J, et al; FAIR-HF Trial Investigators. Ferric carboxymaltose in patients with heart failure and iron deficiency. *N Engl J Med.* 2009;361:2436–2448. doi: 10.1056/NEJMoa0908355
9. Ponikowski P, van Veldhuisen DJ, Comin-Colet J, Ertl G, Komajda M, Mareev V, McDonagh T, Parkhomenko A, Tavazzi L, Levesque V, et al; CONFIRM-HF Investigators. Beneficial effects of long-term intravenous iron therapy with ferric carboxymaltose in patients with symptomatic heart failure and iron deficiency†. *Eur Heart J.* 2015;36:657–668. doi: 10.1093/eurheartj/ehu385
10. van Veldhuisen DJ, Ponikowski P, van der Meer P, Metra M, Böhm M, Doletsky A, Voors AA, Macdougall IC, Anker SD, Roubert B, et al; EFFECT-HF Investigators. Effect of ferric carboxymaltose on exercise capacity in patients with chronic heart failure and iron deficiency. *Circulation.* 2017;136:1374–1383. doi: 10.1161/CIRCULATIONAHA.117.027497
11. Dautry-Varsat A. Receptor-mediated endocytosis: the intracellular journey of transferrin and its receptor. *Biochimie.* 1986;68:375–381. doi: 10.1016/s0300-9084(86)80004-9
12. Mayle KM, Le AM, Kamei DT. The intracellular trafficking pathway of transferrin. *Biochim Biophys Acta.* 2012;1820:264–281. doi: 10.1016/j.bbagen.2011.09.009
13. Boucrot E, Saffarian S, Massol R, Kirchhausen T, Ehrlich M. Role of lipids and actin in the formation of clathrin-coated pits. *Exp Cell Res.* 2006;312:4036–4048. doi: 10.1016/j.yexcr.2006.09.025
14. Merrifield CJ, Kaksonen M. Endocytic accessory factors and regulation of clathrin-mediated endocytosis. *Cold Spring Harb Perspect Biol.* 2014;6:a016733. doi: 10.1101/cshperspect.a016733
15. Patel VB, Zhabyeyev P, Chen X, Wang F, Paul M, Fan D, McLean BA, Basu R, Zhang P, Shah S, et al. PI3Kalpha-regulated gelsolin activity is a critical determinant of cardiac cytoskeletal remodeling and heart disease. *Nat Commun.* 2018;9:5390. doi: 10.1038/s41467-018-07812-8
16. Shah S, Yogasundaram H, Basu R, Wang F, Paterson DI, Alastalo TP, Oudit GY. Novel dominant-negative mutation in cardiac Troponin I causes severe restrictive cardiomyopathy. *Circ Heart Fail.* 2017;10:e003820. doi: 10.1161/CIRCHEARTFAILURE.116.003820
17. McNally EM, Golbus JR, Puckelwartz MJ. Genetic mutations and mechanisms in dilated cardiomyopathy. *J Clin Invest.* 2013;123:19–26. doi: 10.1172/JCI62862
18. Herman DS, Lam L, Taylor MR, Wang L, Teekakirikul P, Christodoulou D, Conner L, DePalma SR, McDonough B, Sparks E, et al. Truncations of titin causing dilated cardiomyopathy. *N Engl J Med.* 2012;366:619–628. doi: 10.1056/NEJMoa1110186
19. Schultheiss HP, Fairweather D, Caforio ALP, Escher F, Hershberger RE, Lipshultz SE, Liu PP, Matsumori A, Mazzanti A, McMurray J, et al. Dilated cardiomyopathy. *Nat Rev Dis Primers.* 2019;5:32. doi: 10.1038/s41572-019-0084-1
20. Chang AN, Potter JD. Sarcomeric protein mutations in dilated cardiomyopathy. *Heart Fail Rev.* 2005;10:225–235. doi: 10.1007/s10741-005-5252-6
21. Sun N, Yazawa M, Liu J, Han L, Sanchez-Freire V, Abilez OJ, Navarrete EG, Hu S, Wang L, Lee A, et al. Patient-specific induced pluripotent stem cells as a model for familial dilated cardiomyopathy. *Sci Transl Med.* 2012;4:130ra–13147. doi: 10.1126/scitranslmed.3003552

22. Wu H, Lee J, Vincent LG, Wang Q, Gu M, Lan F, Churko JM, Sallam KI, Matsa E, Sharma A, et al. Epigenetic regulation of phosphodiesterases 2A and 3A underlies compromised beta-adrenergic signaling in an iPSC model of dilated cardiomyopathy. *Cell Stem Cell*. 2015;17:89–100. doi: 10.1016/j.stem.2015.04.020
23. Dai Y, Amenov A, Ignatyeva N, Koschinski A, Xu H, Soong PL, Tiburcy M, Linke WA, Zaccolo M, Hasenfuss G, et al. Troponin destabilization impairs sarcomere-cytoskeleton interactions in iPSC-derived cardiomyocytes from dilated cardiomyopathy patients. *Sci Rep*. 2020;10:209. doi: 10.1038/s41598-019-56597-3
24. Li D, Czernuszewicz GZ, Gonzalez O, Tapscott T, Karibe A, Durand JB, Brugada R, Hill R, Gregoritch JM, Anderson JL, et al. Novel cardiac troponin T mutation as a cause of familial dilated cardiomyopathy. *Circulation*. 2001;104:2188–2193. doi: 10.1161/hc4301.098285
25. Dieseldorff Jones KM, Koh Y, Weller RS, Turna RS, Ahmad F, Huke S, Knollmann BC, Pinto JR, Hwang HS. Pathogenic troponin T mutants with opposing effects on myofilament Ca. *Arch Biochem Biophys*. 2019;661:125–131. doi: 10.1016/j.abb.2018.11.006
26. Xu H, Wali R, Cheruiyot C, Bodenschatz J, Hasenfuss G, Janshoff A, Habeck M, Ebert A. Non-negative blind deconvolution for signal processing in a CRISPR-edited iPSC-cardiomyocyte model of dilated cardiomyopathy. *FEBS Lett*. 2021;595:2544–2557. doi: 10.1002/1873-3468.14189
27. Matyushenko AM, Levitsky DI. Molecular mechanisms of pathologies of skeletal and cardiac muscles caused by point mutations in the tropomyosin genes. *Biochemistry (Mosc)*. 2020;85:S20–S33. doi: 10.1134/S0006297920140023
28. Gupte TM, Haque F, Gangadharan B, Sunitha MS, Mukherjee S, Anandhan S, Rani DS, Mukundan N, Jambekar A, Thangaraj K, et al. Mechanistic heterogeneity in contractile properties of α-tropomyosin (TPM1) mutants associated with inherited cardiomyopathies. *J Biol Chem*. 2015;290:7003–7015. doi: 10.1074/jbc.M114.596676
29. Chang AN, Harada K, Ackerman MJ, Potter JD. Functional consequences of hypertrophic and dilated cardiomyopathy-causing mutations in alpha-tropomyosin. *J Biol Chem*. 2005;280:34343–34349. doi: 10.1074/jbc.M505014200
30. Tardiff JC. Thin filament mutations: developing an integrative approach to a complex disorder. *Circ Res*. 2011;108:765–782. doi: 10.1161/CIRCRESAHA.110.224170
31. Chang AN, Greenfield NJ, Singh A, Potter JD, Pinto JR. Structural and protein interaction effects of hypertrophic and dilated cardiomyopathic mutations in alpha-tropomyosin. *Front Physiol*. 2014;5:460. doi: 10.3389/fphys.2014.00460
32. Bai F, Groth HL, Kawai M. DCM-related tropomyosin mutants E40K/E54K over-inhibit the actomyosin interaction and lead to a decrease in the number of cycling cross-bridges. *PLoS One*. 2012;7:e47471. doi: 10.1371/journal.pone.0047471
33. Lakdawala NK, Dellefave L, Redwood CS, Sparks E, Cirino AL, Depalma S, Colan SD, Funke B, Zimmerman RS, Robinson P, et al. Familial dilated cardiomyopathy caused by an alpha-tropomyosin mutation: the distinctive natural history of sarcomeric dilated cardiomyopathy. *J Am Coll Cardiol*. 2010;55:320–329. doi: 10.1016/j.jacc.2009.11.017
34. Richardson DR, Lane DJ, Becker EM, Huang ML, Whitnall M, Suryo Rahmanto Y, Sheftel AD, Ponka P. Mitochondrial iron trafficking and the integration of iron metabolism between the mitochondrion and cytosol. *Proc Natl Acad Sci U S A*. 2010;107:10775–10782. doi: 10.1073/pnas.0912925107
35. Kremastinos DT, Farmakis D. Iron overload cardiomyopathy in clinical practice. *Circulation*. 2011;124:2253–2263. doi: 10.1161/CIRCULATIONAHA.111.050773
36. Xu W, Barrientos T, Mao L, Rockman HA, Sauve AA, Andrews NC. Lethal cardiomyopathy in mice lacking transferrin receptor in the heart. *Cell Rep*. 2015;13:533–545. doi: 10.1016/j.celrep.2015.09.023
37. Chen G, Gulbranson DR, Hou Z, Bolin JM, Ruotti V, Probasco MD, Smuga-Otto K, Howden SE, Diol NR, Propson NE, et al. Chemically defined conditions for human iPSC derivation and culture. *Nat Methods*. 2011;8:424–429. doi: 10.1038/nmeth.1593
38. Ebert AD, Kodo K, Liang P, Wu H, Huber BC, Riegler J, Churko J, Lee J, de Almeida P, Lan F, et al. Characterization of the molecular mechanisms underlying increased ischemic damage in the aldehyde dehydrogenase 2 genetic polymorphism using a human induced pluripotent stem cell model system. *Sci Transl Med*. 2014;6:255ra–25130. doi: 10.1126/scitranslmed.3009027
39. Lian X, Hsiao C, Wilson G, Zhu K, Hazeltine LB, Azarin SM, Raval KK, Zhang J, Kamp TJ, Palecek SP. Robust cardiomyocyte differentiation from human pluripotent stem cells via temporal modulation of canonical Wnt signaling. *Proc Natl Acad Sci U S A*. 2012;109:E1848–E1857. doi: 10.1073/pnas.1200250109
40. Lian X, Zhang J, Azarin SM, Zhu K, Hazeltine LB, Bao X, Hsiao C, Kamp TJ, Palecek SP. Directed cardiomyocyte differentiation from human pluripotent stem cells by modulating Wnt/beta-catenin signaling under fully defined conditions. *Nat Protoc*. 2013;8:162–175. doi: 10.1038/nprot.2012.150
41. Atanassov I, Urlaub H. Increased proteome coverage by combining PAGE and peptide isoelectric focusing: comparative study of gel-based separation approaches. *Proteomics*. 2013;13:2947–2955. doi: 10.1002/pmic.201300035
42. Zhang Y, Bilbao A, Bruderer T, Luban J, Strambio-De-Castillia C, Lisacek F, Hopfgartner G, Varesio E. The use of variable Q1 isolation windows improves selectivity in LC-SWATH-MS acquisition. *J Proteome Res*. 2015;14:4359–4371. doi: 10.1021/acs.jproteome.5b00543
43. Lambert JP, Ivosev G, Couzens AL, Larsen B, Taipale M, Lin ZY, Zhong Q, Lindquist S, Vidal M, Aebersold R, et al. Mapping differential interactomes by affinity purification coupled with data-independent mass spectrometry acquisition. *Nat Methods*. 2013;10:1239–1245. doi: 10.1038/nmeth.2702
44. Mann HB, Whitney DR. On a test of whether one of 2 random variables is stochastically larger than the other. *Ann Math Stat*. 1947;18:50–60. doi: 10.1214/aoms/1177730491
45. Hammond GR, Fischer MJ, Anderson KE, Holdich J, Koteci A, Balla T, Irvine RF. PI4P and PI(4,5)P2 are essential but independent lipid determinants of membrane identity. *Science*. 2012;337:727–730. doi: 10.1126/science.1222483
46. Wilhelmi T, Xu X, Tan X, Hulshoff MS, Maamari S, Sossalla S, Zeisberg M, Zeisberg EM. Serelaxin alleviates cardiac fibrosis through inhibiting endothelial-to-mesenchymal transition via RXFP1. *Theranostics*. 2020;10:3905–3924. doi: 10.7150/thno.38640
47. Brandenburg S, Kohl T, Williams GS, Gusev K, Wagner E, Rog-Zielinska EA, Hebisch E, Dura M, Didié M, Gotthardt M, et al. Axial tubule junctions control rapid calcium signaling in atria. *J Clin Invest*. 2016;126:3999–4015. doi: 10.1172/JCI88241
48. Berulava T, Buchholz E, Elerdashvili V, Pena T, Islam MR, Lbik D, Mohamed BA, Renner A, von Lewinski D, Sacherer M, et al. Changes in m6A RNA methylation contribute to heart failure progression by modulating translation. *Eur J Heart Fail*. 2020;22:54–66. doi: 10.1002/ejhf.1672
49. Voigt N, Li N, Wang Q, Wang W, Trafford AW, Abu-Taha I, Sun Q, Wieland T, Ravens U, Nattel S, et al. Enhanced sarcoplasmic reticulum Ca2+ leak and increased Na+-Ca2+ exchanger function underlie delayed afterdepolarizations in patients with chronic atrial fibrillation. *Circulation*. 2012;125:2059–2070. doi: 10.1161/CIRCULATIONAHA.111.067306
50. Ebert AD, Laussmann M, Wegehingel S, Kaderali L, Erfle H, Reichert J, Lechner J, Beer HD, Pepperkok R, Nickel W. Tec-kinase-mediated phosphorylation of fibroblast growth factor 2 is essential for unconventional secretion. *Traffic*. 2010;11:813–826. doi: 10.1111/j.1600-0854.2010.01059.x
51. Matsa E, Burridge PW, Yu KH, Ahrens JH, Termglinchan V, Wu H, Liu C, Shukla P, Sayed N, Churko JM, et al. Transcriptome profiling of patient-specific human iPSC-Cardiomyocytes predicts individual drug safety and efficacy responses in vitro. *Cell Stem Cell*. 2016;19:311–325. doi: 10.1016/j.stem.2016.07.006
52. Garfinkel AC, Seidman JG, Seidman CE. Genetic pathogenesis of hypertrophic and dilated cardiomyopathy. *Heart Fail Clin*. 2018;14:139–146. doi: 10.1016/j.hfc.2017.12.004
53. Yuan CC, Kazmierczak K, Liang J, Zhou Z, Yadav S, Gomes AV, Irving TC, Szczesna-Cordary D. Sarcomeric perturbations of myosin motors lead to dilated cardiomyopathy in genetically modified. *Proc Natl Acad Sci U S A*. 2018;115:E2338–E2347. doi: 10.1073/pnas.1716925115
54. Sequeira V, Nijenkamp LL, Regan JA, van der Velden J. The physiological role of cardiac cytoskeleton and its alterations in heart failure. *Biochim Biophys Acta*. 2014;1838:700–722. doi: 10.1016/j.bbamem.2013.07.011
55. Hein S, Kostin S, Heling A, Maeno Y, Schaper J. The role of the cytoskeleton in heart failure. *Cardiovasc Res*. 2000;45:273–278. doi: 10.1016/s0008-6363(99)00268-0
56. Olson TM, Illenberger S, Kishimoto NY, Huttelmaier S, Keating MT, Jockusch BM. Metavinculin mutations alter actin interaction in dilated cardiomyopathy. *Circulation*. 2002;105:431–437. doi: 10.1161/hc0402.102930
57. Jockusch BM, Isenberg G. Interaction of alpha-actinin and vinculin with actin: opposite effects on filament network formation. *Proc Natl Acad Sci U S A*. 1981;78:3005–3009. doi: 10.1073/pnas.78.5.3005
58. Bois PR, Borgon RA, Vonrhein C, Izard T. Structural dynamics of alpha-actinin-vinculin interactions. *Mol Cell Biol*. 2005;25:6112–6122. doi: 10.1128/MCB.25.14.6112-6122.2005

59. Bois PR, O'Hara BP, Nietlispach D, Kirkpatrick J, Izard T. The vinculin binding sites of talin and alpha-actinin are sufficient to activate vinculin. *J Biol Chem.* 2006;281:7228–7236. doi: 10.1074/jbc.M510397200
60. Sun Y, Martin AC, Drubin DG. Endocytic internalization in budding yeast requires coordinated actin nucleation and myosin motor activity. *Dev Cell.* 2006;11:33–46. doi: 10.1016/j.devcel.2006.05.008
61. Sirotkin V, Beltzner CC, Marchand JB, Pollard TD. Interactions of WASp, myosin-I, and verprolin with Arp2/3 complex during actin patch assembly in fission yeast. *J Cell Biol.* 2005;170:637–648. doi: 10.1083/jcb.200502053
62. Merrifield CJ, Qualmann B, Kessels MM, Almers W. Neural Wiskott Aldrich Syndrome Protein (N-WASP) and the Arp2/3 complex are recruited to sites of clathrin-mediated endocytosis in cultured fibroblasts. *Eur J Cell Biol.* 2004;83:13–18. doi: 10.1078/0171-9335-00356
63. van den Bout I, Divecha N. PIP5K-driven PtdIns(4,5)P2 synthesis: regulation and cellular functions. *J Cell Sci.* 2009;122:3837–3850. doi: 10.1242/jcs.056127
64. Silachev DN, Khailova LS, Babenko VA, Gulyaev MV, Kovalchuk SI, Zorova LD, Plotnikov EY, Antonenko YN, Zorov DB. Neuroprotective effect of glutamate-substituted analog of gramicidin A is mediated by the uncoupling of mitochondria. *Biochim Biophys Acta.* 2014;1840:3434–3442. doi: 10.1016/j.bbagen.2014.09.002
65. Roth MG. Integrating actin assembly and endocytosis. *Dev Cell.* 2007;13:3–4. doi: 10.1016/j.devcel.2007.06.005
66. Antonescu CN, Aguet F, Danuser G, Schmid SL. Phosphatidylinositol-(4,5)-bisphosphate regulates clathrin-coated pit initiation, stabilization, and size. *Mol Biol Cell.* 2011;22:2588–2600. doi: 10.1091/mbc.E11-04-0362
67. Kadlecova Z, Spielman SJ, Loerke D, Mohanakrishnan A, Reed DK, Schmid SL. Regulation of clathrin-mediated endocytosis by hierarchical allosteric activation of AP2. *J Cell Biol.* 2017;216:167–179. doi: 10.1083/jcb.201608071
68. Uribe-Querol E, Rosales CP. Our current understanding of a universal biological process. *Front Immunol.* 2020;11:1066. doi: 10.3389/fimmu.2020.01066
69. Cerri S, Milanese C, Mastroberardino PG. Endocytic iron trafficking and mitochondria in Parkinson's disease. *Int J Biochem Cell Biol.* 2019;110:70–74. doi: 10.1016/j.biocel.2019.02.009
70. Braymer JJ, Lill R. Iron-sulfur cluster biogenesis and trafficking in mitochondria. *J Biol Chem.* 2017;292:12754–12763. doi: 10.1074/jbc.R117.787101
71. Stehling O, Sheftel AD, Lill R. Chapter 12 Controlled expression of iron-sulfur cluster assembly components for respiratory chain complexes in mammalian cells. *Methods Enzymol.* 2009;456:209–231. doi: 10.1016/S0076-6879(08)04412-1
72. Hoes MF, Grote Beverborg N, Kijlstra JD, Kuipers J, Swinkels DW, Giepmans BNG, Rodenburg RJ, van Veldhuisen DJ, de Boer RA, van der Meer P. Iron deficiency impairs contractility of human cardiomyocytes through decreased mitochondrial function. *Eur J Heart Fail.* 2018;20:910–919. doi: 10.1002/ejhf.1154
73. Yanatori I, Kishi F. DMT1 and iron transport. *Free Radic Biol Med.* 2019;133:55–63. doi: 10.1016/j.freeradbiomed.2018.07.020
74. Rhee JW, Yi H, Thomas D, Lam CK, Belbachir N, Tian L, Qin X, Malisa J, Lau E, Paik DT, et al. Modeling secondary iron overload cardiomyopathy with human induced pluripotent stem cell-derived cardiomyocytes. *Cell Rep.* 2020;32:107886. doi: 10.1016/j.celrep.2020.107886
75. Melenovsky V, Petrak J, Mracek T, Benes J, Borlaug BA, Nuskova H, Pluhacek T, Spatenka J, Kovalcikova J, Drahota Z, et al. Myocardial iron content and mitochondrial function in human heart failure: a direct tissue analysis. *Eur J Heart Fail.* 2017;19:522–530. doi: 10.1002/ejhf.640
76. Shibasaki Y, Ishihara H, Kizuki N, Asano T, Oka Y, Yazaki Y. Massive actin polymerization induced by phosphatidylinositol-4-phosphate 5-kinase in vivo. *J Biol Chem.* 1997;272:7578–7581. doi: 10.1074/jbc.272.12.7578
77. Oude Weernink PA, Schulte P, Guo Y, Wetzel J, Amano M, Kaibuchi K, Haverland S, Voss M, Schmidt M, Mayr GW, et al. Stimulation of phosphatidylinositol-4-phosphate 5-kinase by Rho-kinase. *J Biol Chem.* 2000;275:10168–10174. doi: 10.1074/jbc.275.14.10168
78. Lauriol J, Keith K, Jaffré F, Couvillon A, Saci A, Goonasekera SA, McCarthy JR, Kessinger CW, Wang J, Ke Q, et al. RhoA signaling in cardiomyocytes protects against stress-induced heart failure but facilitates cardiac fibrosis. *Sci Signal.* 2014;7:ra100. doi: 10.1126/scisignal.2005262
79. Ronan B, Flamand O, Vescovi L, Dureuil C, Durand L, Fassy F, Bachelot MF, Lamberton A, Mathieu M, Bertrand T, et al. A highly potent and selective Vps34 inhibitor alters vesicle trafficking and autophagy. *Nat Chem Biol.* 2014;10:1013–1019. doi: 10.1038/nchembio.1681
80. Richardson D, Ponka P, Baker E. The effect of the iron(III) chelator, desferrioxamine, on iron and transferrin uptake by the human malignant melanoma cell. *Cancer Res.* 1994;54:685–689.
81. Obejero-Paz CA, Yang T, Dong WQ, Levy MN, Brittenham GM, Kuryshev YA, Brown AM. Deferoxamine promotes survival and prevents electrocardiographic abnormalities in the gerbil model of iron-overload cardiomyopathy. *J Lab Clin Med.* 2003;141:121–130. doi: 10.1067/mlc.2003.18
82. Glickstein H, El RB, Link G, Breuer W, Konijn AM, Hershko C, Nick H, Cabantchik ZI. Action of chelators in iron-loaded cardiac cells: Accessibility to intracellular labile iron and functional consequences. *Blood.* 2006;108:3195–3203. doi: 10.1182/blood-2006-05-020867
83. Jia D, Gomez TS, Metlagel Z, Umetani J, Otwinowski Z, Rosen MK, Billadeau DD. WASH and WAVE actin regulators of the Wiskott-Aldrich syndrome protein (WASP) family are controlled by analogous structurally related complexes. *Proc Natl Acad Sci U S A.* 2010;107:10442–10447. doi: 10.1073/pnas.0913293107
84. Kamisago M, Sharma SD, DePalma SR, Solomon S, Sharma P, McDonough B, Smoot L, Mullen MP, Woolf PK, Wigle ED, et al. Mutations in sarcomere protein genes as a cause of dilated cardiomyopathy. *N Engl J Med.* 2000;343:1688–1696. doi: 10.1056/NEJM200012073432304
85. Ikeda Y, Ross J. Models of dilated cardiomyopathy in the mouse and the hamster. *Curr Opin Cardiol.* 2000;15:197–201. doi: 10.1097/00001573-200005000-00013
86. Nonaka M, Morimoto S. Experimental models of inherited cardiomyopathy and its therapeutics. *World J Cardiol.* 2014;6:1245–1251. doi: 10.4330/wjc.v6.i12.1245
87. Yutzey KE, Robbins J. Principles of genetic murine models for cardiac disease. *Circulation.* 2007;115:792–799. doi: 10.1161/CIRCULATIONAHA.106.682534
88. Rudolph F, Fink C, Hüttemeister J, Kirchner M, Radke MH, Lopez Carballo J, Wagner E, Kohl T, Lehnart SE, Mertins P, et al. Deconstructing sarcomeric structure-function relations in titin-BioID knock-in mice. *Nat Commun.* 2020;11:3133. doi: 10.1038/s41467-020-16929-8
89. Swist S, Unger A, Li Y, Vöge A, von Frieling-Salewsky M, Skärlén A, Cacciani N, Braun T, Larsson L, Linke WA. Maintenance of sarcomeric integrity in adult muscle cells crucially depends on Z-disc anchored titin. *Nat Commun.* 2020;11:4479. doi: 10.1038/s41467-020-18131-2
90. Sah VP, Minamisawa S, Tam SP, Wu TH, Dorn GW 2nd, Ross J Jr, Chien KR, Brown JH. Cardiac-specific overexpression of RhoA results in sinus and atrioventricular nodal dysfunction and contractile failure. *J Clin Invest.* 1999;103:1627–1634. doi: 10.1172/JCI6842
91. Bao W, Hu E, Tao L, Boyce R, Mirabile R, Thudium DT, Ma XL, Willette RN, Yue TL. Inhibition of Rho-kinase protects the heart against ischemia/reperfusion injury. *Cardiovasc Res.* 2004;61:548–558. doi: 10.1016/j.cardiores.2003.12.004
92. Shimizu T, Liao JK. Rho kinases and cardiac remodeling. *Circ J.* 2016;80:1491–1498. doi: 10.1253/circj.CJ-16-0433
93. Surma M, Wei L, Shi J. Rho kinase as a therapeutic target in cardiovascular disease. *Future Cardiol.* 2011;7:657–671. doi: 10.2217/fca.11.51
94. Xiang SY, Vanhoutte D, Del Re DP, Purcell NH, Ling H, Banerjee I, Bossuyt J, Lang RA, Zheng Y, Matkovich SJ, et al. RhoA protects the mouse heart against ischemia/reperfusion injury. *J Clin Invest.* 2011;121:3269–3276. doi: 10.1172/JCI44371
95. Loncar G, Obradovic D, Thiele H, von Haehling S, Lainscak M. Iron deficiency in heart failure. *ESC Heart Fail.* 2021;8:2368–2379. doi: 10.1002/ehf2.13265
96. Torti FM, Torti SV. Regulation of ferritin genes and protein. *Blood.* 2002;99:3505–3516. doi: 10.1182/blood.v99.10.3505
97. Nemeth E, Tuttle MS, Powelson J, Vaughn MB, Donovan A, Ward DM, Ganz T, Kaplan J. Hepcidin regulates cellular iron efflux by binding to ferroportin and inducing its internalization. *Science.* 2004;306:2090–2093. doi: 10.1126/science.1104742
98. Donovan A, Lima CA, Pinkus JL, Pinkus GS, Zon LI, Robine S, Andrews NC. The iron exporter ferroportin/Slc40a1 is essential for iron homeostasis. *Cell Metab.* 2005;1:191–200. doi: 10.1016/j.cmet.2005.01.003
99. Rouault TA. The role of iron regulatory proteins in mammalian iron homeostasis and disease. *Nat Chem Biol.* 2006;2:406–414. doi: 10.1038/nchembio807
100. Sato T, Chang HC, Bayeva M, Shapiro JS, Ramos-Alonso L, Kouzu H, Jiang X, Liu T, Yar S, Sawicki KT, et al. mRNA-binding protein tristetraprolin is essential for cardiac response to iron deficiency by regulating mitochondrial function. *Proc Natl Acad Sci U S A.* 2018;115:E6291–E6300. doi: 10.1073/pnas.1804701115
101. Mordi IR, Tee A, Lang CC. Iron therapy in heart failure: ready for prime-time?. *Card Fail Rev.* 2018;4:28–32. doi: 10.15420/cfr.2018:6:2
102. Serbanovic-Canic J, Cvejic A, Soranzo N, Stemple DL, Ouwehand WH, Freson K. Silencing of RhoA nucleotide exchange factor, ARHGEF3,

reveals its unexpected role in iron uptake. *Blood*. 2011;118:4967–4976. doi: 10.1182/blood-2011-02-337295
103. Zhang H, Zhabyeyev P, Wang S, Oudit GY. Role of iron metabolism in heart failure: From iron deficiency to iron overload. *Biochim Biophys Acta Mol Basis Dis*. 2019;1865:1925–1937. doi: 10.1016/j.bbadis.2018.08.030
104. Zhou J, Ng B, Ko NSJ, Fiedler LR, Khin E, Lim A, Sahib NE, Wu Y, Chothani SP, Schafer S, et al. Titin truncations lead to impaired cardiomyocyte autophagy and mitochondrial function in vivo. *Hum Mol Genet*. 2019;28:1971–1981. doi: 10.1093/hmg/ddz033
105. Galata Z, Kloukina I, Kostavasili I, Varela A, Davos CH, Makridakis M, Bonne G, Capetanaki Y. Amelioration of desmin network defects by αB-crystallin overexpression confers cardioprotection in a mouse model of dilated cardiomyopathy caused by LMNA gene mutation. *J Mol Cell Cardiol*. 2018;125:73–86. doi: 10.1016/j.yjmcc.2018.10.017
106. Lan F, Lee AS, Liang P, Sanchez-Freire V, Nguyen PK, Wang L, Han L, Yen M, Wang Y, Sun N, et al. Abnormal calcium handling properties underlie familial hypertrophic cardiomyopathy pathology in patient-specific induced pluripotent stem cells. *Cell Stem Cell*. 2013;12:101–113. doi: 10.1016/j.stem.2012.10.010
107. Burridge PW, Matsa E, Shukla P, Lin ZC, Churko JM, Ebert AD, Lan F, Diecke S, Huber B, Mordwinkin NM, et al. Chemically defined generation of human cardiomyocytes. *Nat Methods*. 2014;11:855–860. doi: 10.1038/nmeth.2999
108. Malkovskiy AV, Ignatyeva N, Dai Y, Hasenfuss G, Rajadas J, Ebert A. Integrated Ca(2+) flux and AFM force analysis in human iPSC-derived cardiomyocytes. *Biol Chem*. 2020;402:113–121. doi: 10.1515/hsz-2020-0212
109. Hendel A, Bak RO, Clark JT, Kennedy AB, Ryan DE, Roy S, Steinfeld I, Lunstad BD, Kaiser RJ, Wilkens AB, et al. Chemically modified guide RNAs enhance CRISPR-Cas genome editing in human primary cells. *Nat Biotechnol*. 2015;33:985–989. doi: 10.1038/nbt.3290
110. Bak RO, Dever DP, Porteus MH. CRISPR/Cas9 genome editing in human hematopoietic stem cells. *Nat Protoc*. 2018;13:358–376. doi: 10.1038/nprot.2017.143
111. Kodo K, Ong SG, Jahanbani F, Termglinchan V, Hirono K, InanlooRahatloo K, Ebert AD, Shukla P, Abilez OJ, Churko JM, et al. iPSC-derived cardiomyocytes reveal abnormal TGF-beta signalling in left ventricular non-compaction cardiomyopathy. *Nat Cell Biol*. 2016;18:1031–1042. doi: 10.1038/ncb3411
112. Richter KN, Revelo NH, Seitz KJ, Helm MS, Sarkar D, Saleeb RS, D'Este E, Eberle J, Wagner E, Vogl C, et al. Glyoxal as an alternative fixative to formaldehyde in immunostaining and super-resolution microscopy. *EMBO J*. 2018;37:139–159. doi: 10.15252/embj.201695709